POLITECNICO DI TORINO
Repository ISTITUZIONALE

Innovative glass sealants for the integration of protonic ceramic electrolysis cells

Original
Innovative glass sealants for the integration of protonic ceramic electrolysis cells / Da Prato, F., Groß-Barsnick, S., Anelli, S., Deibert, W., Albert Meulenberg, W., Ricote, S., Santarelli, M., Smeacetto, F.. - In: JOURNAL OF POWER SOURCES. - ISSN 0378-7753. - 689:(2026), pp. 1-16. [10.1016/j.jpowsour.2026.240816]

Availability:
This version is available at: 11583/3012455 since: 2026-06-27T08:51:17Z

Publisher:
Elsevier

Published
DOI:10.1016/j.jpowsour.2026.240816

Terms of use:

This article is made available under terms and conditions as specified in the corresponding bibliographic description in the repository

Publisher copyright

(Article begins on next page)

20 November 2026

Journal of Power Sources 689 (2026) 240816

Contents lists available at ScienceDirect

Journal of Power Sources

journal homepage: www.elsevier.com/locate/jpowsour

Innovative glass sealants for the integration of protonic ceramic electrolysis cells

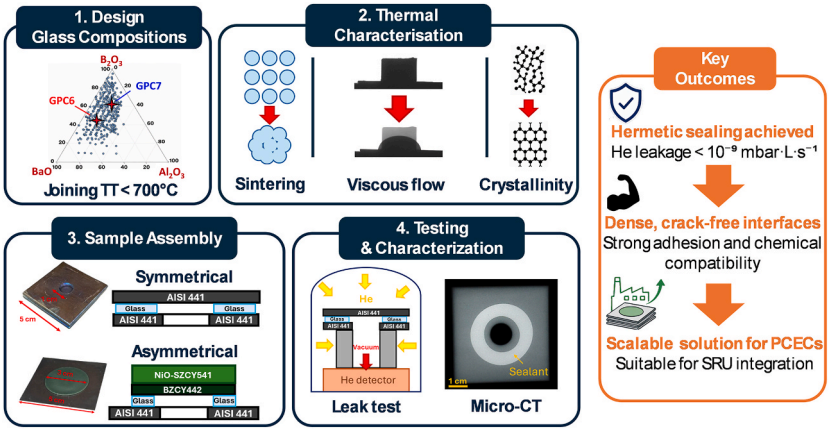
Francesco Da Prato [a,*], Sonja-Michaela Groß-Barsnick [b], Simone Anelli [c], Wendelin Deibert [c], Wilhelm Albert Meulenberg [d], Sandrine Ricote [e], Massimo Santarelli [a], Federico Smeacetto [c]

[a] Department of Energy (DENERG), Politecnico di Torino, Turin, 10129, Italy
[b] Forschungszentrum Jülich GmbH, Institute of Technology and Engineering, ITE, Jülich, 52425, Germany
[c] Department of Applied Science and Technology (DISAT), Politecnico di Torino, Turin, 10129, Italy
[d] Forschungszentrum Jülich GmbH, Institute of Energy Materials and Devices (IMD-2), Jülich, 52425, Germany
[e] HyET NoCarbon, Golden CO80401, CO, USA

HIGHLIGHTS

- Design of innovative glass sealant compositions for PCEC integration.
- Effect of powder morphology on glass viscous flow and crystallisation behaviour.
- Optimisation of joining to ensure gas tightness and control seal geometry.
- Thermochemical compatibility of glass sealants with BZCY half-cells and AISI441.

GRAPHICAL ABSTRACT



ARTICLE INFO

Keywords:
Protonic ceramic cell
Glass sealants
Viscous flow behaviour
Crystallisation kinetics
Joining process optimisation
Gas-tightness

ABSTRACT

This work reports the design, processing, and testing of novel borate-based glass sealants for joining ferritic stainless steel AISI 441 interconnects to NiO-$SrZr_{0.5}Ce_{0.4}Y_{0.1}O_{3-\delta}$ (SZCY541)/$BaZr_{0.44}Ce_{0.36}Y_{0.2}O_{3-\delta}$ (BZCY442) protonic half-cells. Two formulations, belonging to the B_2O_3–BaO–Al_2O_3–CaO–SrO–SiO_2 and B_2O_3–BaO–SiO_2–Al_2O_3–CaO–SrO–ZnO–ZrO_2 systems, are tailored to enable low-temperature joining (<700 °C), thereby limiting interfacial reactivity while ensuring thermomechanical compliance at operating temperatures (≈ 600 °C). The effects of glass chemistry and powder morphology on densification, viscous flow, and crystallisation are systematically investigated, showing predominantly surface-controlled crystallisation behaviour. Screen-printed tapes are used to fabricate symmetric metal/glass/metal assemblies. The joining process is optimised by varying peak temperature and applied pressure to correlate sealant deformation and gas-tightness with processing conditions, defining reliable joining parameters for PCEC stack integration. The resulting

* Corresponding author.
E-mail address: francesco.daprato@polito.it (F. Da Prato).

https://doi.org/10.1016/j.jpowsour.2026.240816
Received 24 April 2026; Received in revised form 5 June 2026; Accepted 23 June 2026
Available online 25 June 2026
0378-7753/© 2026 The Authors. Published by Elsevier B.V. This is an open access article under the CC BY license (http://creativecommons.org/licenses/by/4.0/).

samples show excellent sealing performance, with He leakage rates below 1×10^{-9} mbar L s^{-1} and a final sealant thickness of ≈ 200 μm. Optimised conditions are applied to half-cell/glass/metal joined samples, exhibiting gas-tightness ($\Delta p < 2$ mbar after 5 min) and stable geometry. SEM–EDS confirms strong adhesion and chemical compatibility with NiO–SZCY541/BZCY442 and AISI 441, demonstrating the suitability of the investigated compositions for PCEC sealing.

1. Introduction

In the transition toward a carbon-neutral energy system, green hydrogen is expected to play a central role as both an energy storage medium and an energy carrier in power-to-X schemes [1,2]. In this framework, surplus renewable electricity is converted into hydrogen by electrolysis and can be reconverted into electricity when required [3]. Reliable and efficient electrolysis technologies are therefore essential for large-scale deployment.

High-temperature ceramic electrolysers are particularly attractive because elevated operating temperatures (400–900 °C) enhance electrode kinetics and reduce the required cell voltage, typically to 1.2–1.4 V [4]. This results in lower electrical energy demand compared with low-temperature technologies such as proton exchange membrane electrolysers (PEMECs) and alkaline electrolysers (AECs) [5,6]. Oxygen-ion conducting solid oxide electrolysis cells (SOECs) represent the most mature high-temperature electrolysis technology and are commonly operated at 700–900 °C [7,8]. System-level studies have demonstrated high efficiencies and significant benefits from thermal integration [9]. However, effective heat integration requires steam generation and a dedicated thermal-management architecture. Moreover, large-scale deployment of SOEC technology remains limited by high capital costs and durability issues, mainly related to stack manufacturing complexity, high-temperature balance-of-plant components, and degradation-driven replacement [10–14].

Proton ceramic electrolysis cells (PCECs) have emerged as a promising alternative to SOECs. Unlike SOECs, which rely on oxygen-ion (O^{2-}) transport, PCECs conduct protons (H^{+}) through the electrolyte from the oxygen electrode to the fuel electrode [15]. Proton transport is characterized by relatively low activation energies (0.45–0.65 eV) in the 300–600 °C temperature range [16], enabling efficient operation at intermediate temperatures and potentially mitigating thermally induced degradation phenomena [17–19]. In addition, steam is supplied to the oxygen electrode, while hydrogen is produced at the fuel electrode with limited dilution. This configuration can significantly reduce or eliminate downstream hydrogen separation steps, thereby simplifying system design and offering potential cost and integration advantages [20]. State-of-the-art PCEC electrolytes are based on doped barium cerate–zirconate perovskite solid solutions, $BaZr_{1-x-y}Ce_xM_yO_{3-\delta}$ (BZCM, where M is a trivalent dopant) [21,22]. At the fuel electrode, Ni-based cermets are the most commonly employed fuel-electrode material, typically consisting of metallic Ni combined with a proton-conducting ceramic phase such as BZCM or $SrZr_{1-x-y}Ce_xM_yO_{3-\delta}$ (SZCM) [16]. At the oxygen/steam electrode, mixed ionic–electronic conductors (MIECs), such as $Ba_{1-x}Sr_xCo_{1-y}Fe_yO_{3-\delta}$ (BSCF) and $La_{1-x}Sr_xCo_{1-y}Fe_yO_{3-\delta}$ (LSCF), have been extensively investigated for this application owing to their favourable electrochemical performance [23,24].

Despite the advantages, PCEC technology is still largely confined to the laboratory scale. Most studies focus on materials and cell-level components, while only a limited number address stack design and system integration in both fuel-cell and electrolysis modes [17,25]. The upscaling process requires dedicated investigations at the single-repeating-unit (SRU) level. This includes integrating metallic interconnect plates into the membrane–electrode assembly (MEA) using suitable sealant materials. Ferritic stainless steels (FSSs) already used in SOECs, such as AISI 441, AISI 430, Crofer 22 APU, and Crofer 22 H, have also shown strong potential as interconnect materials for PCECs due to their good oxidation resistance and compatible coefficients of thermal expansion (CTE) [26–28]. Their CTE values, typically 11–12 $\times 10^{-6}$ K^{-1} [29,30] are reasonably well matched with those of doped BZCY perovskites in dry state, which generally range between 8 and 13 $\times 10^{-6}$ K^{-1}, whereas under wet conditions, the apparent thermochemical expansion coefficient is generally lower than the dry-state range and becomes markedly temperature-dependent due to hydration-induced chemical expansion [31]. This effect should be taken into account when evaluating thermo-mechanical compatibility under realistic operating conditions.

For sealing, glass-based materials are the most widely adopted solution. Extensive research has been conducted on glass and glass-ceramic sealants for SOFC and SOEC stack integration [32–35]. These materials offer high compositional flexibility, enabling the tuning of thermomechanical properties to ensure gas-tightness, electrical insulation, and chemical and mechanical compatibility among SRU components. Glass-based sealants typically consist of borosilicate systems containing alkali and alkaline-earth oxides as network modifiers [36], whose sealing behaviour is strongly governed by the balance between viscous flow, densification, and crystallisation during the joining process. Previous studies have shown that the viscosity evolution and crystallisation kinetics must be carefully tailored to allow sufficient wetting and densification before extensive devitrification increases the sealant rigidity and limits flow capability [37–39]. In particular, delayed or controlled crystallisation has been associated with improved joining ability and enhanced thermo-mechanical stability, whereas excessive or premature crystallisation can hinder densification and promote sealing defects [37]. The optimisation of these phenomena is strongly composition-dependent, since network modifiers and intermediate oxides directly affect glass viscosity, crystallisation tendency, and thermal expansion behaviour [40]. Moreover, particle-size distribution plays a critical role in determining sintering kinetics and sealing performance, influencing the densification rate, viscous deformation, and final microstructure of the joined seal [38]. These interrelated effects ultimately govern the relationship between glass composition, microstructural evolution, and joining performance under SOC operating conditions [41–43]. Beyond composition, selecting a suitable deposition technique is equally important. Glass-based sealants are compatible with a wide range of processing methods, including automated techniques such as tape casting, robocasting, and screen printing [44–46]. The choice of deposition strategy, combined with the optimisation of joining temperature and applied pressure, directly affects layer thickness, uniformity, and green density, thereby playing a key role in ensuring process reproducibility and scalability.

In our previous studies, three borosilicate glass compositions, two mainly modified with MgO and one with BaO, originally developed for SOC applications, were also evaluated for PCEC sealing, joining BZCY-based ceramics to an AISI 441 metallic counterpart [47,48]. Two major limitations were identified. First, the relatively high joining temperatures required (800–900 °C) led to interfacial instability during sealing. Second, the elevated glass transition temperatures (T_g) resulted in limited mechanical compliance at typical PCEC operating temperatures (≈600 °C), thereby reducing the sealants' ability to accommodate thermomechanical stresses and promote crack self-healing. Crack formation, driven by CTE mismatch and further aggravated by hydration-induced chemical expansion of BCZY [31,49], highlights the inadequacy of SOC-optimised compositions under PCEC conditions. These findings demonstrate that dedicated glass formulations, specifically engineered for PCEC systems and their associated material

couples, are required. To date, only a limited number of studies have addressed this need. For instance, SiO_2-TiO_2-K_2O-Na_2O-Al_2O_3-ZnO glass sealant was successfully applied to join Mn–Co-coated Crofer 22 H to $BaZr_{0.1}Ce_{0.7}Y_{0.1}Yb_{0.1}O_{3-\delta}$ (BZCYYb), maintaining stability after 300 h in humid oxidizing conditions at 600 °C [28,50–52]. Similarly, borate-rich glasses and a 5 wt% 3YSZ composite formulation demonstrated promising thermal stability when joining BZCY622 to AISI 441 under severe air–steam (70:30 vol%) aging at 600 °C and thermal cycling [47]. However, systematic optimisation of the interrelationship between composition, processing, and joining parameters for PCEC stack integration remains limited.

In this study, innovative borate-rich glass systems were specifically designed as potential sealants to join FSS AISI441 to NiO-$SrZr_{0.5}Ce_{0.4}Y_{0.1}O_{3-\delta}$ (SZCY541)/$BaZr_{0.44}Ce_{0.36}Y_{0.2}O_{3-\delta}$ (BZCY442) half-cells, with a NiO:SZCY541 wt ratio of 60:40 [19,53]. Two formulations belonging to the B_2O_3–BaO–Al_2O_3–CaO–SrO–SiO_2 and B_2O_3–BaO–SiO_2–Al_2O_3–CaO–SrO–ZnO–ZrO_2 systems were developed. Unlike most glass and glass-ceramic sealants reported in the SOC literature, which are predominantly based on silicate or borosilicate networks, the proposed compositions were designed with B_2O_3 as the principal network former and only a limited SiO_2 content. Both formulations have BaO as main glass modifier. This compositional approach was adopted to exploit the intrinsically lower characteristic temperatures of borate-rich glasses, thereby promoting improved wettability and effective joining at temperatures <700 °C, while mitigating interfacial instability phenomena at the glass/ceramic interface. The compositions were further engineered with distinct network modifiers and additives to tailor sintering kinetics and crystallisation behaviour, targeting a predominantly amorphous matrix after joining, with a T_g < 600 °C, to facilitate stress relaxation under PCEC operating conditions, while promoting controlled partial crystallisation to enhance mechanical stability and long-term reliability. Thermal analyses were performed on the proposed systems to systematically investigate sintering and viscous flow behaviour as a function of glass composition and particle size. Based on prior experience in SOC stack assembly at Forschungszentrum Jülich, screen printing was selected as the reference deposition technique. Screen-printed tapes were used to fabricate 5 cm × 5 cm symmetric joined samples (metal/glass/metal) under different peak joining temperatures and applied pressures. The influence of the joining conditions on CTE evolution and crystallisation behaviour was analysed. The joined samples were evaluated for gas tightness, control of sealant width and thickness after joining, and optimal processing parameters were identified. Asymmetric joined samples (ceramic/glass/metal) were subsequently fabricated under the optimised conditions using 3 cm diameter half-cells. These assemblies exhibited excellent gas tightness. Post-mortem SEM–EDS analyses confirmed chemical compatibility at the glass/ceramic and glass/metal interfaces, demonstrating the suitability of the proposed glass systems for PCEC integration at the SRU level.

2. Experimental

2.1. Glass synthesis

Two glass compositions, designed at Politecnico di Torino using the SciGlass® database, were investigated in this study. The first belongs to the B_2O_3–BaO–Al_2O_3–CaO–SrO–SiO_2 system and is internally designated as Glass Proton Ceramic #6 (GPC6). The second, labelled Glass Proton Ceramic #7 (GPC7) is based on the B_2O_3–BaO–SiO_2–Al_2O_3–CaO–SrO–ZnO–ZrO_2 system. Both are barium borate-rich glasses, with B_2O_3 as the main network former and BaO as the primary network modifier. The two compositions differ mainly in the SiO_2 molar content and in the addition of ZnO and ZrO_2 in GPC7. In particular, the higher SiO_2 content in GPC7 was introduced to increase glass network rigidity and viscosity [36], while ZnO and ZrO_2 were added to promote controlled crystallisation [54]. Due to confidentiality constraints, the formulations are reported in Table 1 as molar percentages ranges of the constituent oxides.

For glass synthesis, the appropriate amounts of precursor powders (acids, oxides and carbonates; all from Sigma-Aldrich, purity >99.99%) were weighed into a cylindrical polyethylene (PE) bottle and mixed for 24 h using a roll mixer (RS-TR 5/10, Phoenix Instrument, USA). The batch was then transferred to a Rh–Pt crucible and melted in a chamber furnace (Nabertherm GmbH, Germany) at 1350 °C for 1 h with the lid in place, followed by 30 min at 1400 °C without the lid. The melt was quenched on a brass plate. Each melt yielded approximately 20 g of bulk glass. Ten melts were prepared for each composition, resulting in approximately 200 g of GPC6 and 200 g of GPC7. For each composition, two cast glass droplets (7–8 mm in diameter and 5–6 mm in height) were collected for dilatometry analysis, while the remaining bulk glass was crushed and processed into powders.

2.2. Chemical composition analysis

The chemical composition of the produced glass powders was verified by inductively coupled plasma-optical emission spectroscopy (ICP-OES; iCAP 7600, Thermo Fisher Scientific, USA). Approximately 50 mg of powder was digested in an Au crucible by alkaline fusion using 500 mg NaOH at 600 °C for 30 min. The melt was dissolved in water, transferred, mixed with 25 mL of 5 wt% HCl, and diluted to a final volume of 50 mL. The resulting solutions were analysed semi-quantitatively for the elements of interest.

2.3. Powder processing

Two powder fractions with different particle size distributions (PSD) and specific surface area (SSA) were prepared. To obtain the coarse fraction, 100 g of each glass was dry milled for 1.5 h using a vibratory zirconia mortar grinder (Pulverisette 0, Fritsch GmbH, Germany) with one 50 mm zirconia ball. The powders were then sieved through a 63 μm stainless-steel mesh and labelled GPC6-coarse and GPC7-coarse. The remaining 100 g of each glass was further processed to obtain finer powders. After dry milling, the powders were wet milled in a polyethylene (PE) bottle using ethanol as the milling medium and 3 mm zirconia balls as the grinding media. The powder-to-balls mass ratio was 1:5, and an ethanol-to-powder ratio was 2 mL g^{-1}. Wet milling was performed in a tumbling mixer (Turbula T2F, Willy A. Bachofen AG, Switzerland) for 24 h at 49 rpm. The slurry was dried at 60 °C for 12 h, and the resulting powders were collected and labelled GPC6-fine and GPC7-fine. All processed glass powders were characterized in terms of PSD by static laser scattering (LA-950V2, HORIBA Europe GmbH, Germany) and SSA by nitrogen adsorption (Area Meter II, Juwe Laborgeräte GmbH, Germany).

2.4. Thermal analysis

Glass sintering and viscous-flow behaviour were investigated by hot-stage microscopy (HSM; Hesse Heating Microscope, Germany). Cylindrical pellets (2 mm diameter, 2 mm height) were uniaxially pressed

Table 1
Molar percentage ranges of the constituent oxides in the GPC6 and GPC7 glass systems.

Oxides	GPC6(mol. %)	GPC7 (mol. %)
B_2O_3	30 – 40%	30 – 40%
BaO	30 – 40%	30 – 40%
SiO_2	<5%	5 – 15%
Al_2O_3	5 – 15%	<5%
CaO	5 – 15%	<5%
SrO	<5%	<5%
ZnO	-	<5%
ZrO_2	-	<5%

from the glass powders and placed on NiO–SZCY541/BZCY442 half-cell substrates. The samples were heated in static air from 20 to 300 °C at 10 °C·min^{-1}, then from 300 °C to the melting temperature at 2 °C·min^{-1}. The evolution of pellet shape during heating was recorded with a CCD camera (Leica Microsystem, Germany). The images were used to determine characteristic temperatures associated with sintering, viscous flow, and wetting on the substrate. These characteristic temperatures were used to construct the apparent viscosity–temperature curves using the Vogel–Fulcher–Tammann (VFT) equation [55].

Differential scanning calorimetry (DSC 404 F3 Pegasus, NETZSCH, Germany) was carried out on glass powders with different particle sizes. For each run, approximately 30 mg of powder was loaded into a Pt crucible and heated from 20 to 1000 °C with heating rates of 5, 10, 20, and 30 °C·min^{-1}. Air was used as purge gas (50 mL·min^{-1}), while N_2 was used as a protective gas (20 mL·min^{-1}). Before each measurement, a baseline run was recorded with an empty Pt crucible under identical conditions and subtracted from the sample signal. T_g, crystallisation onset temperature (T_x), and crystallisation peak temperature (T_p) were extracted from the DSC curves. Non-isothermal crystallisation kinetics were analysed using the Ozawa and Matusita–Sakka methods [56–58] to estimate the apparent activation energy (E_a), the Avrami exponent (n), and the crystal growth dimensionality (m), as a function of glass composition and particle size. To evaluate the rate-limiting steps governing crystallisation, E_a was finally compared with the activation energy of viscous flow (E_η) [59–61].

Dilatometry was used to measure the dilatometric softening temperature (T_d) and the CTE of the designed glass systems. Measurements were performed using a dilatometer (DIL 402 PC, NETZSCH, Germany) at 5 °C·min^{-1} from room temperature to the softening point. The CTE was calculated between 100 and 500 °C by linear regression of the dilatometric strain curves, with the CTE corresponding to the slope of the fitted line. *R-square* value was reported for each fit. CTE of the as-cast glasses was tested using bulk droplets collected after quenching. To evaluate the CTE after the joining thermal treatments, powder pellets were uniaxially pressed under a 2.5 t load and heated to the selected peak joining temperatures for 30 min with a heating rate of 2 °C·min^{-1}.

2.5. Joining process optimisation

Fig. 1 summarizes the workflow adopted for the joining-process optimisation. The procedure included preparation of green sealant tapes (Fig. 1a), fabrication of symmetric and asymmetric joined samples (Fig. 1b), gas-tightness evaluation (Fig. 1c), and characterisation of the final seal geometry by micro-computed tomography (micro-CT) (Fig. 1d).

2.5.1. Joining assembly

Sealant pastes were prepared by mixing GPC6–coarse and GPC7–coarse glass powders with an organic solvent and a binder solution according to a patented formulation [62]. The pastes were screen-printed onto a plastic tape-casting carrier foil using a circular-ring pattern (AT-60PD, ESC GmbH, Germany) to a final thickness of approximately 500 μm. The printed layers were dried at 60 °C for 12 h to obtain green sealant tapes. Ring-shaped green tapes (Fig. 1a) were produced by punching the layers with a metal die (inner diameter of 24 mm, outer diameter of 29 mm) and used to assemble symmetric and asymmetric samples (Fig. 1b). Symmetrical joined samples were assembled using two 50 mm × 50 mm × 3 mm AISI 441 plates (Aperam Stainless Services & Solutions, Italy), only one of which contained a central hole with a diameter of 1 mm. Between the two FSS plates, 150 μm-thick 3YSZ tape spacers were inserted to impose a minimum sealant thickness, previously identified as required to prevent electrical short circuits between the plates [37]. Dead loads were applied to provide the target joining pressure. In the first set of symmetric joined samples, the joining pressure was fixed at 0.02 MPa and three peak joining temperatures were tested: 640, 650, and 670 °C for GPC6–coarse, and 660, 680, and 690 °C for GPC7–coarse. Joining was performed in static air using a furnace (Nabertherm 1300, Nabertherm GmbH, Germany). A debinding step was applied at 350 °C for 1 h and 550 °C for 1 h. Heating and cooling rates were fixed at 2 °C·min^{-1} for all samples, consistent with typical SOFC/SOEC start-up and shut-down ramps [63]. Based on previous studies, the dwell time at the peak joining temperature was 30 min [47]. In the second set of symmetric samples, the joining pressure was varied at a fixed peak joining temperature. For GPC6–coarse, the peak temperature was set to 670 °C; while for GPC7–coarse it was set to 690 °C. Joining pressures of 0.005, 0.01, and 0.02 MPa were applied. Asymmetric joined samples were fabricated at 670 °C for 30 min under 0.005 MPa for GPC6–coarse, and at 690 °C for 30 min under 0.01 MPa for GPC7–coarse. The asymmetric joined samples were assembled using NiO–SZCY541/BZCY442 half-cells

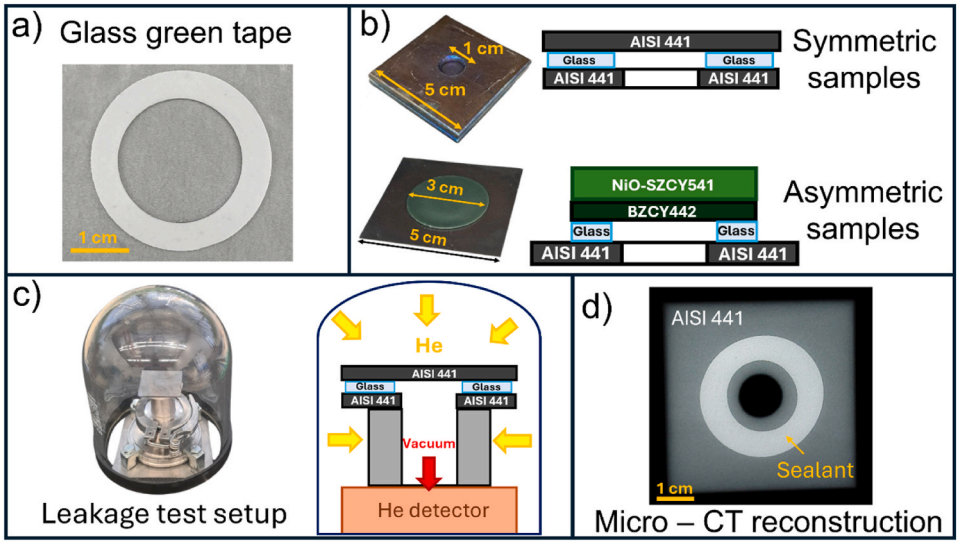


Fig. 1. Workflow adopted for joining-process optimisation. (a) Digital photograph of the ring-shaped screen-printed green glass tape used to assemble symmetric and asymmetric joined samples. (b) Digital photograph and schematic illustration of the symmetric joined samples configuration used for joining-process optimisation. (c) Digital photograph and schematic of the helium leak-testing setup used to evaluate the gas tightness of the symmetric joined samples. (d) Top-view micro-CT reconstruction of a symmetric joined sample used to extract the final sealant geometric parameters. (For interpretation of the references to colour in this figure legend, the reader is referred to the Web version of this article.)

(30 mm diameter, 0.5 mm thick; IMD-2, Forschungszentrum Jülich) and AISI 441 plates (50 mm × 50 mm × 3 mm) with a central 1 mm diameter hole.

2.5.2. Leakage test

To assess the integrity of the joined samples and the absence of critical defects after the corresponding joining thermal treatment, gas-tightness of symmetrically joined samples was measured at room temperature using a custom setup (Fig. 1c). Each sample was placed in a sealed glass chamber purged with helium (He) to impose a 1 bar pressure difference. The internal volume of the joined sample was connected through the central hole to a vacuum line and evacuated. Helium permeating through the sealant was quantified for 45 min using a helium leak detector (UL200, INFICON). Gas-tightness of asymmetrically joined samples was evaluated using a custom pressure-drop station. A pressure of 150 mbar was applied through the central hole in the AISI 441 plate, and the pressure decay over 5 min, associated with leakage through the glass sealant, was recorded using a manometer (WIKA indicator A-AS-1).

2.5.3. Microstructural characterisation

Crystallinity evolution after the joining thermal treatments was evaluated by X-ray diffraction (XRD; D4 ENDEAVOR, Bruker AXS GmbH, Germany). Phase identification was performed using X'Pert HighScore (Malvern Panalytical, United Kingdom) and ICDD/JCPDS reference files. Joining integrity and sealant deformation were evaluated by X-ray computed tomography (micro-CT) using an X-RAY Worx XWT-300-CT Plus microfocus tube coupled with a PerkinElmer XRD 1611 detector, operated at 128 kV and 0.487 mA with an exposure time of 1 s. Specifically, sealant width was measured on micro-CT reconstructions of the joined samples using Fiji (ImageJ; National Institutes of Health, Bethesda, MD, USA). For each sample, 10 measurements were taken along the entire ring geometry, and the results were reported as mean values with standard deviation. Sealant thickness was calculated from the difference between the symmetric sample thickness before and after the joining thermal treatment. Measurements were performed at 10 different positions, and mean values with standard deviation were reported. Post-mortem microstructural analyses were performed on cross-sections of the asymmetric joined samples by field-emission scanning electron microscopy (FE-SEM; MIRA3 XMH TESCAN, Czech Republic) coupled with energy-dispersive X-ray spectroscopy (EDS; UltimMAX 40, Oxford Instruments, United Kingdom). Samples were embedded in epoxy resin (Struers, Denmark), sectioned using a precision diamond saw (TM2200, ATM Qness GmbH, Germany), re-embedded, and polished using SiC abrasive papers of decreasing grit size down to 1 μm. Finally, the surfaces were sputter-coated with a 3 nm platinum layer (ZEISS, Germany) to improve electrical conductivity.

3. Results and discussion

3.1. Chemical characterisation

The selected sealants, labelled GPC6 and GPC7, are barium borate-rich glasses, where B_2O_3 is the main glass network former and BaO is the main glass network modifier. Pure B_2O_3 glasses are mainly built from trigonal BO_3 units arranged in six-membered boroxol rings (B_3O_6). This structure results in a relatively open and less rigid network, which lowers glass viscosity and improves wetting of the joining surfaces at lower temperatures than silicate glasses [64]. Accordingly, parent borate-rich glasses exhibit lower T_g and T_s, allowing sealing below 700 °C, which our previous study identified as the maximum joining temperature to suppress interfacial instability at the glass/perovskite interface [47], while ensuring adequate stability for PCEC operation between 400 and 600 °C. Pure B_2O_3 glasses have a CTE of approximately 14×10^{-6} K^{-1} [36], providing a suitable base for CTE matching with AISI 441 ($11–12 \times 10^{-6}$ K^{-1}) and doped BZCY perovskites ($8–13 \times 10^{-6}$ K^{-1}). Moreover, they exhibit extremely low nucleation rates, as homogeneous nucleation typically occurs well below T_g, where viscosity is too high for crystal growth [65]. This favours the retention of an amorphous phase after joining, which can potentially promote crack self-healing during operation and mitigate stresses associated with chemical expansion in hydrated perovskites. However, excessive amorphous content may weaken mechanical stability and promote viscous flow at operating temperature. Glass modifiers are therefore required to balance viscosity, crystallisation tendency, and mechanical stability. Different glass modifiers were added (Table 1), and BaO was selected as the main one. In borate-rich glasses, BaO addition initially induces the conversion of trigonal BO_3 units into tetrahedral BO_4 units, increasing network connectivity, viscosity, and characteristic temperatures [66]. Above a threshold concentration (≈35 mol. % in the binary BaO-B_2O_3 systems [67]), further BaO addition leads to the formation of non-bridging oxygens, reducing network polymerisation, viscosity, and thermal stability, while enhancing the tendency toward crystallisation [68]. Therefore, the B_2O_3/BaO ratio was carefully tuned to control both viscosity and crystallisation behaviour, which are key factors for sealant densification and long-term performance.

Nevertheless, B_2O_3-rich glasses may undergo composition changes during melting, primarily due to volatilisation of borate-containing species and gas-phase association reactions [69]. Mass-spectrometric studies on multicomponent borosilicate glasses show that borate-derived species can dominate the vapour phase in B_2O_3-rich glass systems. Vapour speciation and partial pressures are governed by the oxide inventory and by acid–base interactions in the melt. These studies also indicate that low-volatility oxides, such as Al_2O_3 and alkaline-earth oxides (e.g., CaO), can decrease the relative volatility and modify the vapour speciation [70]. Volatilisation may therefore reduce compositional control during melting and shift the glass from its designed formulation, with potential implications for the thermo-mechanical and chemical properties required for reliable joining. For these reasons, the as-cast glasses were chemically verified by ICP-OES to quantify deviations from the designed formulation. The results are summarized in Table 2 and are reported as relative deviations (Δ%) of the measured molar concentrations from the theoretical values to preserve formulation confidentiality.

As demonstrated by the ICP-OES analyses, no relevant compositional changes were detected in the cast glasses. All oxides showed only small relative deviations, which are mainly attributed to experimental uncertainties in precursor weighing and batch preparation. No significant B_2O_3 volatilisation was observed, as indicated by the minimal deviations for B_2O_3 (−0.1% for GPC6 and −0.5% for GPC7). These results confirm that the adopted melting and casting thermal treatment is suitable for investigating glass systems.

3.2. Powder processing

Fig. 2a and b compare the PSDs and representative SEM micrographs of GPC6 (both coarse and fine) and GPC7 (both coarse and fine),

Table 2
ICP-OES compositional analysis of the GPC6 and GPC7 glass systems, reported as relative deviations (Δ%) between measured and theoretical molar concentrations.

Oxide	Δ% GPC6	Δ% GPC7
B_2O_3	−0.1	−0.5
SiO_2	+1.8	+2.3
Al_2O_3	+3.0	+2.9
BaO	−2.3	−0.1
CaO	+0.5	+1.8
SrO	−1.1	−0.5
ZnO	-	−1.5
ZrO_2	-	−2.1

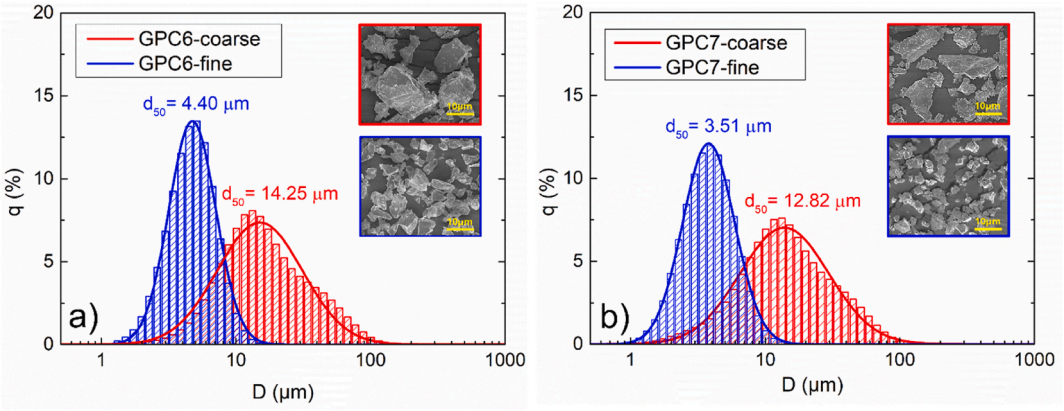


Fig. 2. Particle size distributions (PSD) of the processed glass powders. (a) GPC6-coarse and GPC6-fine; (b) GPC7-coarse and GPC7-fine. Insets show representative SEM micrographs of the corresponding powder morphologies.

respectively.

With optimised powder processing, both systems exhibit a monomodal PSD. This is important for comparing crystallisation kinetics and sintering/viscous-flow behaviour without the additional complexity of bimodal or strongly skewed distributions. As shown in Fig. 2, for both compositions, the fine fraction is shifted toward smaller particle sizes and shows a narrower distribution with shorter tails than the coarse fraction. This confirms the effectiveness of the additional wet-milling step. The SEM micrographs are consistent with the PSD results. Coarse powders contain larger, more angular particles and display a pronounced coarse tail. In contrast, fine powders are finer and more homogeneous. The d_{10}, d_{50}, and d_{90} values, together with the SSA measured by nitrogen adsorption, are reported in Table 3.

Overall, the reduction in characteristic particle size from coarse to fine increases the SSA by a factor of approximately 6 for GPC6 and approximately 4 for GPC7, and is expected to enhance surface-driven phenomena [71]. The coarse fraction was targeted to match the PSD/SSA range required for screen-printing pastes [62], which is the deposition technique adopted in this work. The fine fraction was produced as a contrasting morphology to quantify morphology-driven effects on densification and crystallisation, and its PSD/SSA also falls within the typical range for robocasting or tape-casting inks [44]. Although these deposition techniques are not used here, the thermal analyses obtained for the fine powders remain directly applicable to joining process optimisation when sealant layers are deposited by robocasting or tape casting.

3.3. Sintering behaviour

Fig. 3a and b shows the shrinkage curves (A/A_0, %) as a function of T (°C) obtained by HSM analyses. The measurements were performed on GPC6-coarse and GPC6-fine (Fig. 3a) and on GPC7-coarse and GPC7-fine (Fig. 3b) glass pellets, on BZCY442 half-cell substrates. From these curves, the following characteristic temperatures were determined: (1) the first shrinkage temperature (T_{fs}) and (2) the maximum shrinkage temperature (T_{ms}), corresponding to the onset of linear shrinkage and the temperature at which the maximum shrinkage is reached, respectively; (3) the softening temperature (T_s), at which the first evidence of softening is observed; (4) the sphere temperature (T_b) defined as the temperature at which the sample height equals the base width; (5) the half-sphere temperature (T_{hb}) at which the sample height is half the base width; and (6) the flowing temperature (T_m), at which the sample height decreases to less than one-third of the base width [72]. Table 4 summarizes these characteristic temperatures for both glass systems.

From Fig. 3 and Table 4, GPC7 exhibits systematically higher characteristic temperatures than GPC6. This trend is consistent with the lower B_2O_3/SiO_2 ratio of GPC7, which increases network connectivity and, consequently, glass viscosity [36]. Accordingly, T_{fs} and T_{ms} are 10–15 °C higher for GPC7 than for GPC6 for both powder fractions. The shift is more pronounced at softening, with T_s increasing by 15–20 °C from GPC6 to GPC7. For GPC7, positioning T_s 15–20 °C above the intended PCEC operating temperature (≈600 °C) is advantageous, as it limits viscous deformation during operation, thereby mitigating sealant squeeze-out and helping to preserve the seal geometry. Above the softening point, where viscous flow becomes the dominant deformation mechanism, the divergence between GPC6 and GPC7 is largely governed by crystallisation. In the HSM profiles, crystallisation typically manifests as a plateau, indicating a transient reduction in glass flow as the effective viscosity increases due to crystal nucleation and growth within the glassy matrix [68]. In this respect, GPC6 displays a T_b about 20 °C lower than GPC7 and, crucially, reaches T_{hb} before the crystallisation plateau (≈660–800 °C). Conversely, GPC7 reaches T_{hb} after its crystallisation plateau (680–770 °C). This different sequence of viscous flow relative to crystallisation leads to a markedly higher T_{hb} for GPC7, yielding an overall offset of ≈ 100 °C between the two compositions for both powder fractions. A swelling event around T_f is observed in the HSM curves of both powder fractions and is attributed to foaming driven by gas evolution (e.g., CO_2 release) during heating [73]. Regarding the effect of powder morphology on sintering behaviour, the fine powders (*i.e.* higher SSA) exhibit greater shrinkage at a given temperature for both glass compositions. At T_{ms}, the shrinkage is ≈ 30% for the coarse powders and ≈ 40% for the fine powders for both GPC6 and GPC7, indicating that finer powders promote greater densification and a more compact microstructure. Consistently, the onset of densification shifts to lower temperatures for fine powders: T_{fs} and T_{ms} decrease by 10–11 °C for GPC6 and by 6–7 °C for GPC7 when moving from coarse to fine powders. These reductions are consistent with the expected effect of increased SSA, which accelerates viscous-flow sintering kinetics in glass powder compacts [71]. Powder morphology also affects crystallisation, as shown in Fig. 3aand b by differences in the temperature at which the plateau begins for the two particle-size fractions. For GPC6, the plateau starts earlier for the fine fraction (≈ 660 °C) than for the coarse fraction (≈ 670 °C); these temperatures closely match T_{hb}, and both plateaus terminate at similar temperatures (≈ 790 °C). In contrast, for GPC7 the

Table 3
Particle size distribution parameters d_{10}, d_{50},d_{90} and specific surface area (SSA) of the processed GPC6 and GPC7 glass powders. PSD values were obtained by static laser scattering, while SSA values were measured by nitrogen adsorption.

Composition	d_{10} (μm)	d_{50} (μm)	d_{90} (μm)	SSA ($m^2 \cdot g^{-1}$)
GPC6-fine	2.53	4.40	7.19	1.09
GPC6-coarse	6.24	14.25	43.36	0.17
GPC7-fine	1.92	3.51	6.10	1.39
GPC7-coarse	4.91	12.82	37.74	0.32

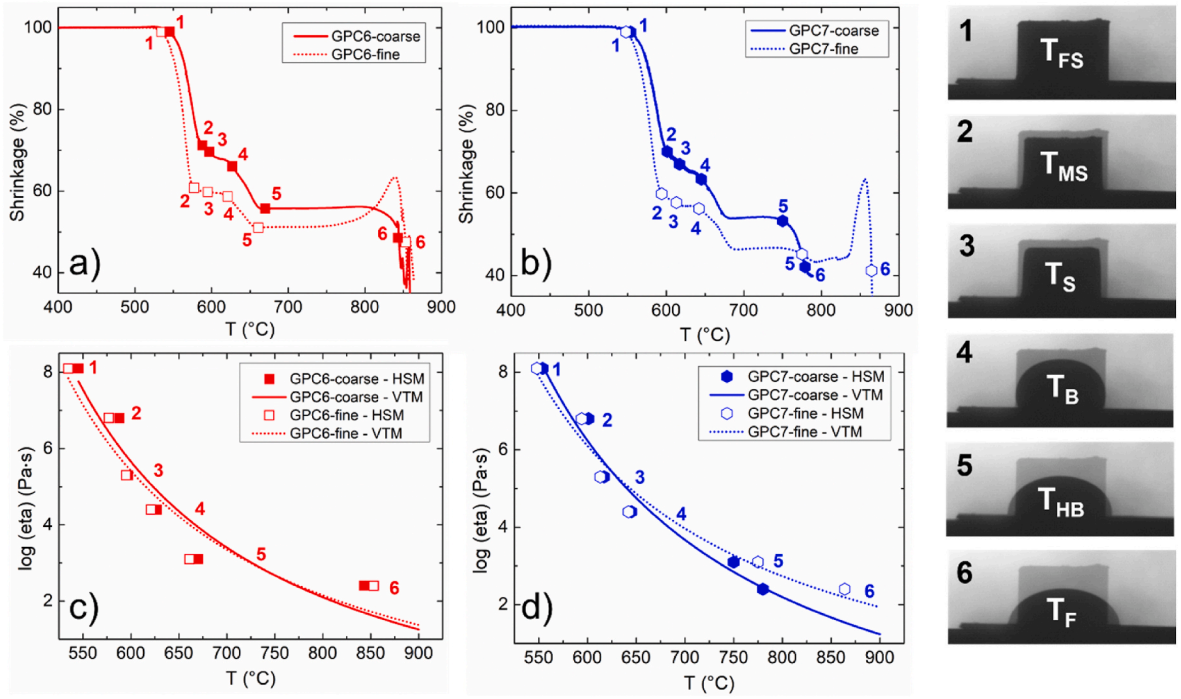


Fig. 3. HSM analysis of GPC6 and GPC7 fine and coarse powder compacts placed on NiO–SZCY541/BZCY442 half-cell substrates and heated in static air from 20 to 300 °C at 10 °C·min^{-1} and from 300 °C to the melting region at 2 °C·min^{-1}. (a) Shrinkage curves of GPC6-coarse and GPC6-fine. (b) Shrinkage curves of GPC7-coarse and GPC7-fine. (c) Estimated apparent log(η)–T curves for GPC6-coarse and GPC6-fine, obtained by fitting HSM-derived fixed-viscosity points. (d) Estimated apparent log(η)–T curves for GPC7-coarse and GPC7-fine, obtained by fitting HSM-derived fixed-viscosity points. The right inset shows representative HSM images corresponding to the characteristic temperatures.

Table 4
HSM-derived characteristic temperatures of GPC6 and GPC7 fine and coarse powder compacts measured on NiO–SZCY541/BZCY442 half-cell substrates in static air.

Glass systems	GPC6-fine	GPC6-coarse	GPC7-fine	GPC7-coarse
T_{fs} (°C)	535	545	548	554
T_{ms} (°C)	577	588	594	601
T_s (°C)	595	597	615	620
T_b (°C)	621	627	642	645
T_{hb} (°C)	661	670	775	750
T_f (°C)	853	843	865	779

plateau onset occurs around 690 °C for the fine fraction and around 680 °C for the coarse fraction. However, the plateau is broader for fine powders, extending to higher temperatures than the corresponding coarse fraction. Overall, these trends indicate that crystallisation kinetics are composition-dependent and further modulated by powder morphology.

Fig. 3c and d report the estimated apparent viscosity–temperature trends for GPC6 (Fig. 3c) and GPC7 (Fig. 3d), comparing coarse and fine powders. The approach proposed by Pascual et al. [72] was adopted to estimate the viscosity behaviour from fixed-viscosity points obtained by HSM. In particular, the characteristic temperatures associated with log $(\eta) < 10$ were fitted by determining the A, B, and T_0 constants of the Vogel–Fulcher–Tammann (VFT) equation:

$$\log(\eta) = A + \frac{B}{T - T_0} \quad (1)$$

The corresponding fitting parameters and R-square values are reported in Table 5.

It should be noted that this approach provides an indirect estimation of the viscosity–temperature dependence, rather than a direct viscosity measurement. Nevertheless, it is useful for comparing the relative

Table 5
Fitting parameters and R-square values of the Vogel–Fulcher–Tammann (VFT) equation obtained from HSM-derived fixed-viscosity points for GPC6 and GPC7 fine and coarse powders.

Glass system	GPC6 – fine	GPC6 – coarse	GPC7 – fine	GPC7 – coarse
A	−0.05	−0.07	−0.2	−2.33
B	903.0	866.8	1169	2003
T_0 (°C)	426.8	441.8	409.3	364.1
R-square	0.941	0.936	0.97	0.967

viscous-flow behaviour of the investigated glass systems, particularly above the softening range, where the HSM-derived characteristic points are most representative [55,74]. Therefore, the estimated curves were used to support the interpretation of the HSM shrinkage profiles and to assess the influence of composition and crystallisation on the viscous-flow behaviour of GPC6 and GPC7. For GPC6, powder morphology has a limited impact on the estimated apparent viscosity at a given temperature, as the coarse and fine curves nearly overlap over the entire investigated range. In contrast, for GPC7, the fine powders show a higher apparent viscosity from ≈ 650 °C onward, consistent with a more pronounced crystallisation, which restricts viscous flow. More generally, GPC7 exhibits higher apparent viscosity than GPC6 at the same temperature. For instance, at 700 °C the estimated viscosity is ≈ $10^{3.4}$ Pa s for both powder fractions of GPC6, ≈ 10^4 Pa s for GPC7-fine, and ≈ $10^{3.7}$ Pa s for GPC7-coarse. The estimated viscosity–temperature curves were finally used to support the identification of the processing window for the joining thermal treatment. To ensure adequate wetting while minimizing squeeze-out, the glass viscosity during joining should fall within approximately $10^{4.5}$ – 10^3 Pa s [75], corresponding to 640–720 °C for GPC6-fine and GPC6-coarse, 670–760 °C for GPC7-fine, and 660–730 °C for GPC7-coarse. Considering that 700 °C was identified as the maximum joining temperature to avoid interfacial instability at the electrolyte/glass interface, the effective processing windows were

therefore restricted to 640–700 °C for GPC6-fine and GPC6-coarse, 670–700 °C for GPC7-fine, and 660–700 °C for GPC7-coarse. These temperature windows were subsequently combined with the crystallisation analysis to define the joining process optimisation.

3.4. Crystallisation behaviour of the glass sealants

Fig. 4a and b presents DSC measurements for GPC6 and GPC7, respectively. From the DSC curves T_g, T_x, T_p were extracted at each heating rate. T_g was determined as the onset of the first endothermic transition (downward step). T_x and T_p were taken as the onset and the maximum of the exothermic peak (upward peak), respectively. The defined T_p were used for non-isothermal determination of crystallisation kinetic parameters. The simplest approach is the Kissinger method, where T_p is measured as a function of α with Eq. (2) [58]:

$$\ln\left(\frac{\alpha}{T_p^2}\right) = \left(\frac{-E_{ak}}{RT_P}\right) + cost \tag{2}$$

Here, E_{ak} is the apparent activation energy obtained by the Kissinger method. It describes the sensitivity of crystallisation to temperature. It is therefore an indicator of the tendency of a glass to crystallize under a given thermal profile (temperature - dwell time - heating rate). The plot of $\ln(\alpha/T_p^2)$ versus $1/T_p$ should be linear and the slope yields E_{ak}. However, Eq. (2) is only valid when crystal growth occurs on a fixed number of nuclei. If nuclei form mainly during the DSC heating run, the number of nuclei changes with α. This occurs because the sample spends different amounts of time within the nucleation temperature range. Under these conditions, Eq. (2) may yield biased activation energies. In this case, the modified Kissinger Eq. (3) proposed by Matusita and Sakka is more appropriate [56]:

$$\ln\left(\frac{\alpha^n}{T_p^2}\right) = \left(\frac{-mE_a}{RT_P}\right) + cost \tag{3}$$

In Eq. (3), E_a is the apparent activation energy for crystallisation calculated by the Matusita–Sakka method. It is obtained by dividing the slope of the linear plot of $\ln(\alpha^n/T_p^2)$ versus $1/T_p$ by the parameter m. The parameter m depends on the dimensionality of crystal growth (e.g., one-, two-, or three-dimensional growth). The exponent n is the Avrami exponent. It reflects the combined nucleation and growth mechanism. It can be determined using the modified Ozawa relation [57]:

$$\left(\frac{d(\ln(-\ln(1-x)))}{d\ln\alpha}\right)_T = -n \tag{4}$$

where x is the crystallized volume fraction at a fixed temperature T. Here, x was calculated from the DSC exothermic peak as the ratio between the partial area up to the selected temperature and the total peak area. The parameters m and n are related by the nucleation conditions. Specifically, $m = n$ when crystallisation at different heating rates occurs on a fixed number of nuclei (site-saturated nucleation). In contrast, $m = n - 1$ when nucleation proceeds during the DSC run and the number of nuclei varies with the heating rate, typically decreasing as α increases.

All characteristic temperatures obtained from the DSC analyses are listed in Table 6. As shown in Fig. 4b, GPC7 exhibits two crystallisation peaks: peak 1 between 700 and 800 °C and peak 2 between 800 and 900 °C. Only peak 1 is reported in Table 6 and used for subsequent analysis, as it falls within the temperature window relevant to the joining thermal treatment.

T_g of GPC6 and GPC7 is approximately 540 °C and 545 °C, respectively. Powder morphology does not significantly affect T_g, as it is primarily governed by glass composition rather than particle size or shape. Both T_g values are suitable for application as sealants in PCEC systems with a target operating temperature of approximately 600 °C. Operating above T_g promotes viscous flow of the residual glassy phase. This can enable self-healing of microcracks formed during operation [36].

As shown in Fig. 4aand b, T_p increases with α for both glass systems and for both powder fractions. This shift reflects the reduced time

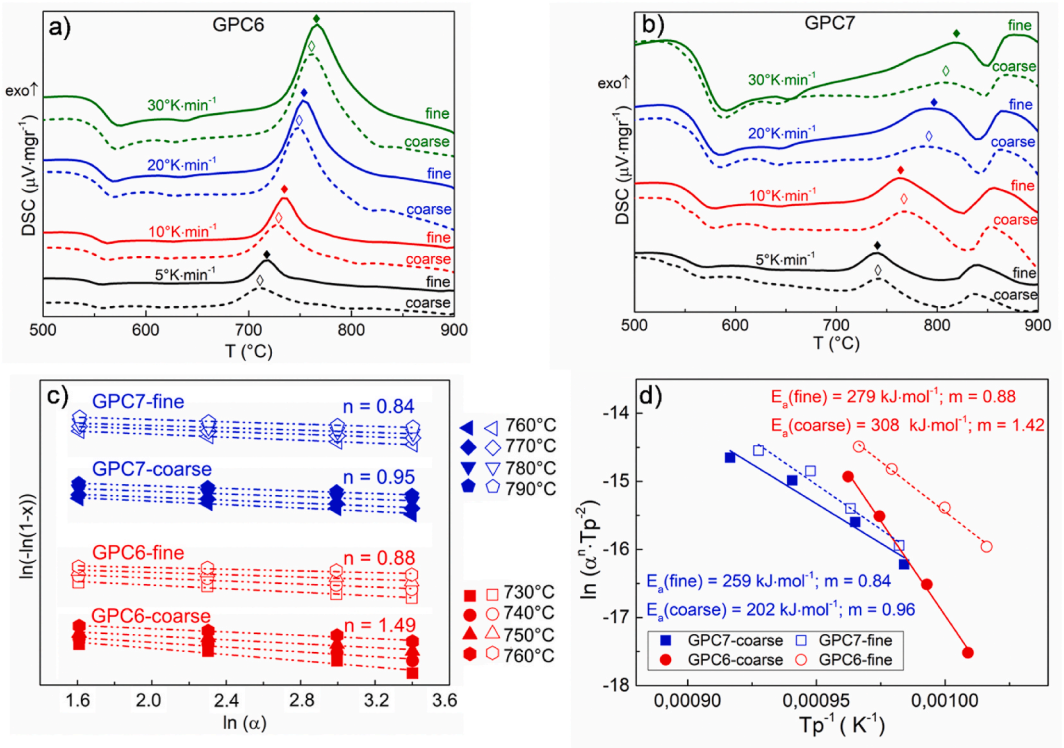


Fig. 4. DSC-based crystallisation kinetic analysis of GPC6 and GPC7 fine and coarse powders. DSC curves of (a) GPC6 and (b) GPC7 were collected at heating rates of 5, 10, 20, and 30 °C·min^{-1}, using air as purge gas and N_2 as protective gas. (c) Ozawa plots evaluated in the 730–760 °C range for GPC6 and in the 760–790 °C range for GPC7, used to determine the Avrami exponent, n. (d) Matusita–Sakka plots used to determine the apparent crystallisation activation energy (E_a) using m = n.

Table 6
T_g, T_x, and T_p values of GPC6 and GPC7 fine and coarse glass powders obtained from DSC measurements performed at heating rates of 5, 10, 20, and 30 °C·min^{-1}, using air as purge gas and N_2 as protective gas.

Glass system	α (°C·min^{-1})	T_g (°C)	T_x (°C)	T_p (°C)
GPC6-fine	5	534	670	711
	10	540	685	727
	20	541	701	748
	30	542	713	762
GPC6-coarse	5	535	689	718
	10	540	702	734
	20	542	720	753
	30	545	726	766
GPC7-fine	5	539	707	745
	10	543	726	765
	20	547	730	782
	30	548	739	805
GPC7-coarse	5	541	708	743
	10	544	723	763
	20	548	736	790
	30	553	745	818

available for nucleation and growth at higher heating rates [76]. For GPC6, the fine powders show lower T_p than the coarse powders at the same α. For GPC7, T_p values are very similar at low heating rates ($\alpha = 5$ and 10 °C·min^{-1}), with the fine fraction slightly higher than the coarse one. At higher heating rates ($\alpha = 20$ and 30 °C·min^{-1}), the fine fraction shows lower T_p than the coarse fraction. In general, T_p depends on the total concentration of nuclei, including both surface and bulk nuclei. T_p decreases as the nuclei concentration increases. Therefore, both bulk and surface crystallisation can occur, although one mechanism may dominate. In these systems, reducing particle size increases the specific surface area and the density of surface nucleation sites. This shifts T_p to lower temperatures, which means predominantly surface-driven crystallisation for both GPC6 and GPC7. If the glass is not initially saturated with bulk nuclei, additional bulk nuclei can form during the DSC heating run. Their concentration is higher at slower heating rates, because the material spends more time in the temperature interval where nucleation is possible. The influence of bulk nucleation is expected to be stronger in larger particles, which provide a larger effective volume for internal nucleation. At low heating rates, powders with different particle sizes are therefore expected to become highly nucleated, thereby minimizing their differences in T_p. As the heating rate increases, bulk nucleation becomes less effective, particularly in larger particles, and the nuclei concentration in coarse powders is expected to decrease. Consequently, the difference in nuclei concentration between fine and coarse powders increases with heating rate. This explains why, for GPC7, T_p values for the fine and coarse fractions are almost identical at low α, whereas at higher α the fine powder shows lower T_p than the coarse powder [77].

Figure S1 (Supplementary Material) reports the Kissinger plot used to calculate the activation energy by the Kissinger method. E_{ak} is 282 kJ mol^{-1} and 303 kJ mol^{-1} for GPC6-fine and GPC6-coarse, respectively, and 262 kJ mol^{-1} and 202 kJ mol^{-1} for GPC7-fine and GPC7-coarse, respectively. Fig. 4c shows the Ozawa plots used to determine the Avrami exponent n. The n values are 0.88 and 1.43 for GPC6-fine and GPC6-coarse, respectively, and 0.84 and 0.95 for GPC7-fine and GPC7-coarse, respectively. Avrami exponents in the range 0.5–1.5 are commonly associated with predominantly surface-controlled crystallisation [78]. These results support the previous interpretation that crystallisation in GPC6 and GPC7 is mainly surface-driven for both fine and coarse powders. The higher n values obtained for the coarse powders indicate a relatively larger bulk contribution compared with the fine fractions, while the overall crystallisation mechanism remains predominantly surface-driven [60]. In predominantly surface-controlled crystallisation of glass powders, crystallisation occurs mainly from pre-existing active sites at the particle surfaces, while the formation of new bulk nuclei during the DSC heating run is typically negligible. This is consistent with previous studies showing that surface crystallisation is primarily governed by particle size, crystal-growth morphology, and the density of active surface nucleation site [59,61]. Under these conditions, crystallisation can be approximated as site-saturated nucleation, where the number of active nuclei remains approximately constant during the DSC run; accordingly, the Matusita–Sakka parameters can be related as $m = n$ [56]. Based on this assumption, the apparent activation energy was derived from the slopes of the Matusita–Sakka plots reported in Fig. 4d. The resulting E_a values are 279 kJ mol^{-1} and 308 kJ mol^{-1} for GPC6-fine and GPC6-coarse, respectively, and 259 kJ mol^{-1} and 201 kJ mol^{-1} for GPC7-fine and GPC7-coarse, respectively. All values are summarized in Table 7.

The two methods provide very similar activation energies for all samples. The relative deviations between E_a and E_{ak} are −1.06% for GPC6-fine, +1.65% for GPC6-coarse, −1.15% for GPC7-fine, and −0.50% for GPC7-coarse. GPC7 shows lower activation energies than GPC6 for both fine and coarse fractions. This indicates a higher tendency to crystallize under the same thermal conditions. The addition of nucleating agents such as ZnO and ZrO_2 has been reported to decrease E_a [54], which is consistent with this trend. A different effect of powder morphology is observed for the two glass systems. In GPC6, E_a is lower for the fine powder than for the coarse one. Conversely, in GPC7, E_a is lower for the coarse powder than for the fine one. The difference may reflect different rate-limiting steps controlling crystallisation in the two systems [61].

To rationalize the differences, E_a was compared with the activation energy for viscous flow (E_η), which represents the apparent energy barrier associated with the structural rearrangements required for viscous flow and thus quantifies the temperature sensitivity of viscosity. Although E_η generally decreases with increasing temperature [59], it can be assumed constant over a limited temperature interval and estimated using an Arrhenius-type relationship:

$$\ln(\eta) = \left(\frac{E_\eta}{RT}\right) + cost \tag{5}$$

where η is the viscosity at temperature T. Accordingly, E_η is obtained from the slope of a linear fit of $\ln(\eta)$ versus $1/T$. When $E_a \approx E_\eta$ within the same temperature range, crystallisation kinetics are typically interpreted as being largely controlled by diffusion/crystal growth coupled to viscosity [79]. Conversely, $E_a > E_\eta$ indicates the presence of additional energetic barriers, most commonly associated with nucleation, contributing to the overall crystallisation rate. The E_η values for GPC6-fine, GPC6-coarse, GPC7-fine, and GPC7-coarse were estimated in the 700–800 °C interval using the viscosity values reported in Fig. 3. The corresponding $\ln(\eta)$ versus $1/T$ plots are provided in Figure S2 (Supplementary Material). For GPC6-coarse, E_η is 127 kJ mol^{-1} while for GPC6-fine is 139 kJ mol^{-1}. This value is much lower than E_a. This indicates that diffusion and crystal growth by viscous flow are not the limiting factors for crystallisation rate in this temperature range. On the other hand, the strong shift of T_x with heating rate (Table 6) suggests that nucleation, rather than growth, controls the crystallisation rate [61]. This interpretation is consistent with the increase of n from 0.88 to 1.43, indicating a stronger bulk contribution in the coarser powder. For GPC7, E_η calculated between 700 and 800 °C are 243 kJ mol^{-1} and

Table 7
Apparent crystallisation activation energies obtained from the Kissinger method, E_{ak}, and from the Matusita–Sakka method, E_a, together with the Avrami exponent, n, and the crystal growth parameter, m.

Glass system	E_{ak} (kJ·mol^{-1})	E_a (kJ·mol^{-1})	n	m
GPC6-fine	282	279	0.88	0.88
GPC6-coarse	303	308	1.43	1.43
GPC7-fine	262	259	0.84	0.84
GPC7-coarse	202	201	0.95	0.95

290 kJ mol^{-1} for fine and coarse powder, respectively. These values are close to, and slightly higher than, E_a. This indicates that crystallisation is more strongly coupled to viscous flow. In this system, diffusion and crystal growth controlled by viscous flow are therefore expected to play a major role in the overall crystallisation rate [61].

Overall, these insights into nucleation and growth mechanisms, combined with the sintering behaviour, are very important and provide a solid basis for optimisation of the joining process. On the one hand, the formation and growth of crystalline phases during the thermal treatment influence glass densification and viscous flow, thereby directly affecting gas tightness and the final seal geometry, including width and thickness. On the other hand, controlling the final degree of crystallisation of the glass sealant after joining is essential, as it governs the CTE evolution, mechanical integrity, thermal stability, and the ability of the residual glassy phase to relax stresses. Furthermore, it is crucial to identify whether crystallisation is predominantly surface- or bulk-controlled because different powder morphologies and particle-size distributions lead to different nucleation site densities and, therefore, different crystallisation extents under an identical thermal profile. Consequently, the same glass composition may develop different viscous flow behaviour and post-joining microstructures when subjected to the same thermal treatment, depending on whether it is processed into powders with morphologies tailored to different deposition techniques, which in turn govern the final mechanical properties of the glass and its ability to accommodate thermally induced stresses.

3.5. Joining process optimisation

Fig. 5a–d shows the XRD patterns and dilatometry curves of GPC6-coarse and GPC7-coarse after the joining thermal treatments, in order to assess the effect of the selected joining thermal profiles on crystallinity evolution and on the CTE and T_d responses, for joining process optimisation.

For GPC6-coarse (Fig. 5a), no crystalline phases are detected after any joining thermal treatments, and the glass remains fully amorphous. For GPC7-coarse (Fig. 5c), the amorphous structure is preserved after 660 °C-30 min, whereas partial devitrification is observed after 680 °C-30 min and becomes more pronounced after 690 °C-30 min, where β–BaB_2O_4 (ICDD 01-085-0914) is identified. This phase has been previously reported in similar borate-rich glass systems [66,80]; its formation is consistent with the surface-controlled crystallisation inferred from the kinetic analysis. The higher devitrification of GPC7-coarse compared with GPC6-coarse is consistent with the higher peak temperatures applied to GPC7-coarse (closer to T_x) and with its lower E_a, in agreement with the trends discussed in the previous section.

Table 8 reports the CTE values calculated by linear fitting of the dilatometric strain curves between 100 and 500 °C, together with the

Table 8
Coefficient of thermal expansion (CTE) values of GPC6 and GPC7 before and after the selected joining thermal treatments, calculated by linear fitting of the dilatometric strain curves in the 100–500 °C range. The corresponding R-square values are reported as an indicator of fit linearity. The literature CTE values of AISI 441 and BZCY442 are included for comparison.

Material	Joining thermal profile	CTE (100-500 °C)	*R-square*
GPC6 after casting	-	11.6 × 10^{-6} K^{-1}	0.99
GPC6 - coarse	640 °C – 30 min	11.6 × 10^{-6} K^{-1}	1
	650 °C – 30 min	11.3 × 10^{-6} K^{-1}	1
	670 °C – 30 min	11.5 × 10^{-6} K^{-1}	1
GPC7 after casting	-	10.4 × 10^{-6} K^{-1}	1
GPC7 - coarse	660 °C – 30 min	10.7 × 10^{-6} K^{-1}	0.98
	680 °C – 30 min	10.6 × 10^{-6} K^{-1}	0.99
	690 °C – 30 min	11.3 × 10^{-6} K^{-1}	0.96
AISI 441	-	11 × 10^{-6} K^{-1}	-
BZCY442	-	10.9 × 10^{-6} K^{-1}	-

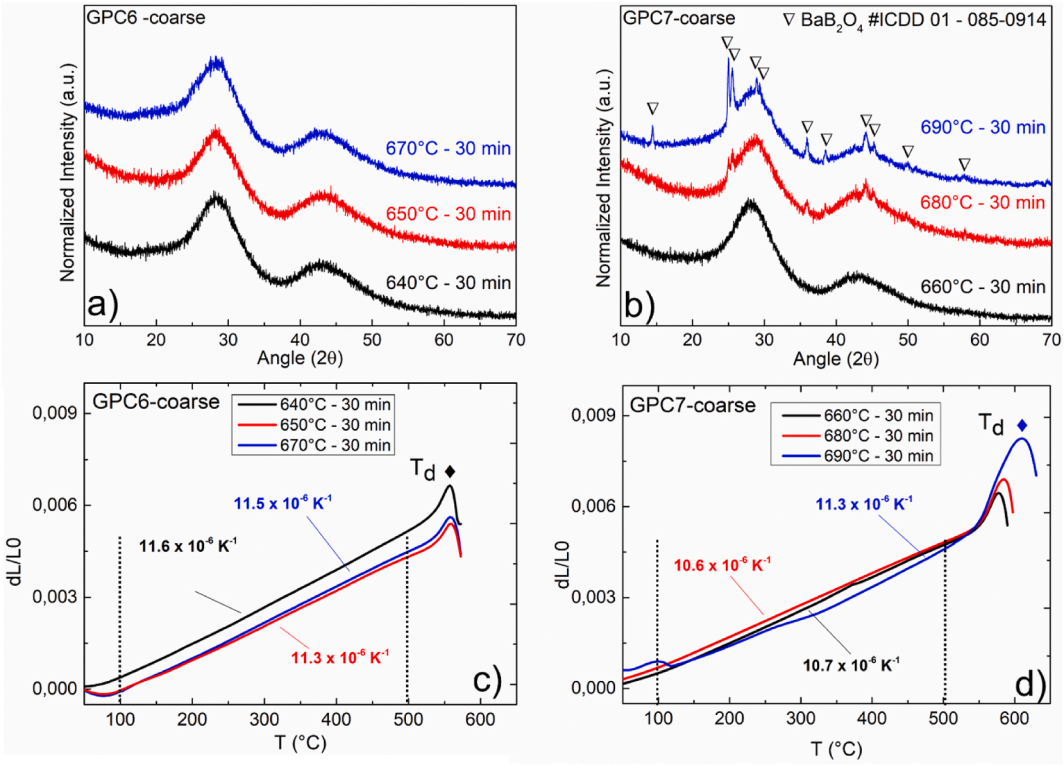


Fig. 5. Crystallinity evolution and dilatometric response of GPC6-coarse and GPC7-coarse after the selected joining thermal treatments. (a) XRD patterns of GPC6-coarse treated at 640, 650, and 670 °C for 30 min. (b) XRD patterns of GPC7-coarse treated at 660, 680, and 690 °C for 30 min. (c) Dilatometry curves of GPC6-coarse after the corresponding thermal treatments, measured from room temperature to the softening region at 5 °C·min^{-1} in static air. (d) Dilatometry curves of GPC7-coarse after the corresponding thermal treatments, measured from room temperature to the softening region at 5 °C·min^{-1} in static air.

corresponding *R-square* values used to assess fit linearity and CTE reliability. The literature CTE values of AISI 441 [30] and BZCY442 [81] are included for comparison.

The CTE of GPC6 and GPC7 after casting, evaluated between 100 and 500 °C, is 11.6 × 10^{-6} K^{-1} and 10.4 × 10^{-6} K^{-1}, respectively. For GPC6-coarse (Fig. 5c), the CTE between 100 and 500 °C remains nearly constant at 11.3–11.5 × 10^{-6} K^{-1} across all thermal profiles, consistent with a fully amorphous structure. For GPC7-coarse (Fig. 5d), the CTE between 100 and 500 °C is 10.7 × 10^{-6} K^{-1} after 660 °C-30 min and 680 °C-30 min, and increases to 11.3 × 10^{-6} K^{-1} after 690 °C-30 min. This variation correlates with the higher crystalline fraction formed at 690 °C. The reported CTE of β-BaB_2O_4 is ≈3 × 10 10^{-6} K^{-1} along the *a* and *b* directions and ≈45 × 10^{-6} K^{-1} along the *c* direction [82], which contributes to the increase of the effective CTE of the glass–ceramic as crystallisation progresses. The slightly lower *R-square* value obtained for GPC7-coarse treated at 690 °C-30 min (*R-square* = 0.96) reflects the moderate deviation from linearity observed in the 100–500 °C fitting range. Nevertheless, this value remains sufficiently high to support the reliability of the calculated CTE. From the dilatometric curves, the dilatometric T_g is identified as the onset of the peak, while T_d corresponds to the peak maximum. T_d marks the deviation from linear elastic behaviour and the onset of progressive loss of rigidity and deformability. It is therefore associated with glass softening in a higher-viscosity regime (≈10^{11} Pa·s) compared with T_s determined by HSM (≈10^8 Pa·s) [55]. The dilatometric T_g values (535 °C for GPC6-coarse and 545 °C for GPC7-coarse, respectively) are in good agreement with DSC results and remain unchanged after the different joining thermal treatments. The T_d of GPC6-coarse remains approximately 560 °C across all thermal profiles. In contrast, the T_d of GPC7-coarse increases from about 575 °C after 660 °C-30 min to 585 °C after 680 °C-30 min, and to approximately 610 °C after 690 °C-30 min. This increase follows the progressive formation of β–BaB_2O_4 and indicates an extension of the linear elastic behaviour temperature range of the GPC7-coarse glass–ceramic, as also reported for other glass–ceramic systems [38,83,84].

Overall, the thermal treatments applied to GPC6-coarse do not induce significant changes in either crystallisation behaviour or CTE. In contrast, for GPC7-coarse, the 690 °C-30 min treatment induces partial crystallisation while preserving a residual amorphous fraction. This microstructural evolution is sufficient to shift the CTE toward values more compatible with AISI 441 ≈ 11–12 × 10^{-6} K^{-1} and BZCY442 perovskite in dry state 10.9 × 10^{-6} K^{-1} [81], while simultaneously increasing T_d. Moreover, it is expected to reduce viscous deformation and increase mechanical stability at high temperatures [85]. Based on that, 690 °C-30 min was selected as the fixed thermal profile for GPC7 in the second optimisation step. For comparison, 670 °C-30 min was selected as the fixed thermal profile for GPC6, corresponding to the highest peak temperature investigated in the first set.

Leakage tests were performed to evaluate the gas tightness of all symmetric samples, and the corresponding He leakage rates (mbar·L·s^{-1}) are reported in Table 9.

Table 9
Room-temperature helium leakage rates of symmetric metal/glass/metal joined samples after the corresponding joining thermal treatments. Measurements were performed using a helium leak detector under a 1 bar pressure difference.

Composition	Joining thermal profile	Joining pressure (MPa)	He leakage rates (mbar·L·s^{-1})
GPC6-coarse	640 °C – 30 min	0.02	1 × 10^{-7}
	650 °C – 30 min	0.02	<1 × 10^{-9}
	670 °C – 30 min	0.02	<1 × 10^{-9}
	670 °C – 30 min	0.01	<1 × 10^{-9}
	670 °C – 30 min	0.005	<1 × 10^{-9}
GPC7-coarse	660 °C – 30 min	0.02	<1 × 10^{-9}
	680 °C – 30 min	0.02	<1 × 10^{-9}
	690 °C – 30 min	0.02	<1 × 10^{-9}
	690 °C – 30 min	0.01	<1 × 10^{-9}
	690 °C – 30 min	0.005	<1 × 10^{-9}

Among the investigated conditions, GPC6-coarse sample joined at 640 °C-30 min under 0.02 MPa shows a gas leakage rate of 1 × 10^{-7} mbar L s^{-1}. All the other samples exhibit gas leakage rates <1 × 10^{-9} mbar L s^{-1}, below the detection limit of the instrument. Although these measurements do not represent high-temperature leakage rates under operating conditions, they provide evidence of effective sealing after joining and are consistent with preliminary gas-tightness requirements for PCC/SOC sealing [40,86]. Within the investigated ranges, no systematic effect of peak joining temperature or applied pressure is observed. These results indicate excellent wettability of both GPC6-coarse and GPC7-coarse at peak joining temperatures <700 °C. To the best of the authors' knowledge, gas-tightness data for glass sealants specifically developed for PCEC integration are absent. For the glass-sealant systems developed for SOC application, tested with the same measurement set-up, leakage rates <1 × 10^{-9} mbar L s^{-1} have been reported for an SrO-MgO-B_2O_3-SiO_2 glass joined for 10 h at 850 °C under 0.02 MPa in metal/glass/metal assemblies using Crofer 22 APU as the metallic counterpart [37]. Similarly, a BaO–CaO–SiO_2–B_2O_3 glass developed for joining $SrTi_{0.75}Fe_{0.25}O_{3-\delta}$ (STF25) oxygen transport membranes to Aluchrom achieved leakage rates <1 × 10^{-9} mbar L s^{-1} in metal/glass/metal joined samples after a 10 h treatment at 850 °C under ~0.02 MPa [87]. Compared with these systems, the GPC6-coarse and GPC7-coarse sealants achieve comparable gas-tightness at significantly lower joining temperatures and shorter dwell times, which are advantageous for minimizing interfacial reactions and reducing thermo-mechanical mismatch during PCEC assembly, and support their suitability for SRU-level integration.

Fig. 6 reports the evolution of the final sealant width and thickness of the symmetric joined samples. Fig. 6a shows the sealant width and thickness for samples assembled with GPC6–coarse and GPC7–coarse as a function of peak joining temperature, at a fixed pressure of 0.02 MPa and a dwell time of 30 min. Fig. 6b displays the final sealant width and thickness as a function of the applied joining pressure, using fixed thermal profiles of 670 °C-30 min for GPC6–coarse and 690 °C-30 min for GPC7–coarse. The corresponding micro-CT reconstructions are shown in Figures S3 and S4 (Supplementary Material).

The final sealant dimensions result from the combined effects of organic burn-out of the screen-printed green tape, volumetric shrinkage during glass sintering, viscous flow, and deformation induced by the applied load during joining. All samples were produced using the same screen-printing paste composition. Therefore, for a given glass composition, the contributions from organic burn-out and intrinsic sintering shrinkage are comparable across the investigated conditions. The analysis thus isolates the effects of peak joining temperature and applied pressure on the control of the final sealant geometry. For GPC6-coarse (Fig. 6a), increasing the peak joining temperature at fixed pressure leads to a progressive decrease in final thickness and a corresponding increase in final width, consistent with enhanced viscous flow. At 670 °C for 30 min, the average width is approximately 7.5 mm. The associated increase in standard deviation indicates pronounced sealant spreading and reduced control of the circular-ring geometry. Under the same conditions, a minimum thickness of about 150 μm is achieved, matching that of the 3YSZ spacers. For GPC7-coarse (Fig. 6b), increasing the peak temperature from 660 °C to 680 °C results in an increase in final width and a decrease in thickness, again consistent with enhanced viscous flow. At 680 °C for 30 min, the sealant reaches a 3YSZ spacer thickness of 150 μm. In contrast, at 690 °C-30 min, an inversion of this trend is observed. The final width decreases, while the thickness increases relative to the 680 °C condition. This behaviour is attributed to the onset of crystallisation in GPC7-coarse, which hinders viscous flow and enables improved control of the final sealant geometry. A direct comparison of the deformation trends indicates that, under the same temperature and pressure, GPC6-coarse would exhibit a higher tendency to spread than GPC7-coarse. This is consistent with the higher T_s and T_d measured for GPC7-coarse by HSM and dilatometry. For both GPC6-coarse and GPC7-coarse, increasing the joining pressure at a fixed

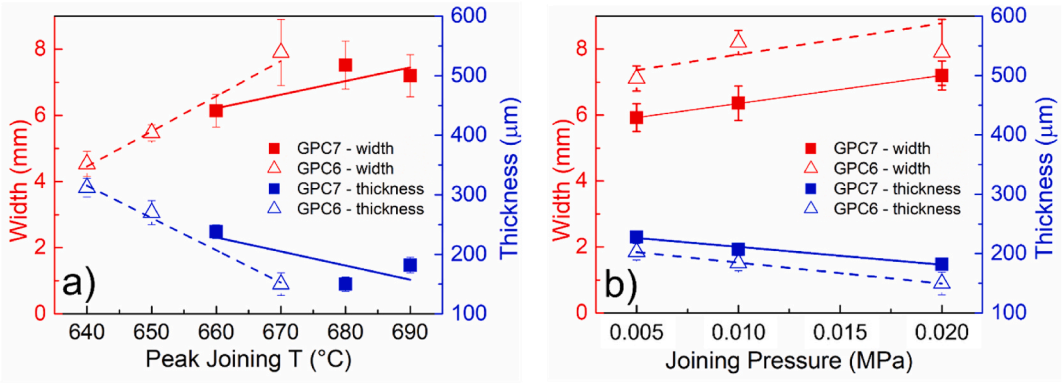


Fig. 6. Final sealant geometry of symmetric metal/glass/metal joined samples evaluated by micro-CT after joining in static air. (a) Sealant width and thickness of GPC6-coarse and GPC7-coarse samples as a function of peak joining temperature, using a fixed joining pressure of 0.02 MPa and a dwell time of 30 min. (b) Sealant width and thickness as a function of applied joining pressure, using fixed thermal treatments of 670 °C for 30 min for GPC6-coarse and 690 °C for 30 min for GPC7-coarse.

thermal profile promotes sealant spreading, resulting in larger final width and lower final thickness (Fig. 6b). No inversion of the trend is observed. At constant temperature, the applied pressure levels do not induce additional crystallisation phenomena, and the deformation remains mainly controlled by viscous flow and load. For GPC6-coarse treated at 670 °C-30 min, reducing the joining pressure to 0.005 MPa improves geometry control, yielding a thickness of approximately 200 µm and a width of about 7 mm, with low dispersion. For GPC7–coarse treated at 690 °C-30 min, the most stable geometry is obtained at 0.01 MPa, with a thickness of approximately 200 µm and a width of about 6.5 mm. These peak temperatures and joining pressures were therefore selected as the optimised conditions in terms of geometric control, particularly because they yield a final sealant thickness of ≈ 200 µm, which is consistent with values typically considered practical in SOCs stack assembly [63].

Fig. 7 shows the micro-CT reconstructions of the asymmetric and symmetric joined samples produced under the optimised conditions of 670 °C for 30 min under 0.005 MPa for GPC6-coarse and 690 °C for 30 min under 0.01 MPa for GPC7-coarse. In all samples, the sealant maintains a regular geometry, with no marked asymmetries associated with excessive spreading. The sealant layer appears continuous and

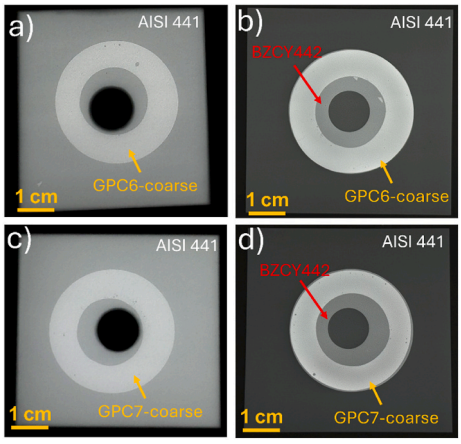


Fig. 7. Top-view micro-CT reconstructions of symmetric and asymmetric joined samples fabricated under optimised joining conditions in static air. (a) Symmetric and (b) asymmetric samples assembled with GPC6-coarse at 670 °C for 30 min under 0.005 MPa. (c) Symmetric and (d) asymmetric samples assembled with GPC7-coarse at 690 °C for 30 min under 0.01 MPa. Yellow arrows indicate the sealant layer, while red arrows indicate the half-cell. (For interpretation of the references to colour in this figure legend, the reader is referred to the Web version of this article.)

crack-free, with no detectable porosity. The slight non-coaxiality between the tape and the hole in the metal plate observed in the symmetric joined samples is attributed to manual sample assembly and does not compromise their functionality.

Gas tightness was further assessed by pressure-drop measurements on the asymmetric joined samples. After 5 min, pressure decreased by 1.8 mbar (GPC6-coarse) and 2.1 mbar (GPC7-coarse), confirming a low leakage rate and an effective hermetic seal. These results support the structural integrity of the samples and indicate excellent wetting and adhesion of the designed borate-rich glasses to the BZCY442 electrolyte when joined at temperatures below 700 °C.

Fig. 8 presents SEM cross-sections and EDS analyses of the GPC6-coarse asymmetric sample joined at 670 °C-30 min under 0.005 MPa and of the GPC7-coarse asymmetric sample joined at 690 °C-30 min under 0.01 MPa.

Fig. 8a shows the AISI 441/GPC6-coarse interface, while Fig. 8e shows the GPC6-coarse/BCZY442 interface. The glass shows good adhesion and continuity at both the electrolyte and interconnect interfaces. The sealant is dense and crack-free, and no relevant residual porosity is observed in the analysed cross-sections. This microstructure is consistent with the extremely low He gas leakage rates measured for the corresponding symmetric joined samples. Fig. 8b and c shows the EDS maps of Fe and Cr, respectively. Within the spatial resolution of EDS, no detectable Fe or Cr diffusion from AISI 441 into the glass is observed after joining. Although BCZY442 contains Ba, the electrolyte appears darker in Fig. 8f because the EDS contrast is relative and was adjusted to emphasise Ba-depleted crystalline regions within the Ba-rich glass.

In Fig. 8a and e, needle-shaped features with darker contrast are present within the glass matrix. These features are attributed to crystalline phases formed during the joining thermal treatment. Their density increases toward the glass/BCZY442 interface (Fig. 8e), indicating preferential crystallisation near the electrolyte surface. No crystalline phases are detected by XRD on the same thermal treated GPC6-coarse powders (Fig. 5a), which reflect an amount below the XRD detection limit (<5 wt%) [88]. However, the local EDS maps indicate a distinct composition for the needle-shaped phase. The Ba signal is reduced (Fig. 8d), while Si and Ca are enriched (Fig. 8f–h). This compositional partitioning suggests the formation of a Ca–silicate phase. No microstructural evidence of interfacial instability or interdiffusion is observed at the glass/BZCY442 interface within the resolution of the SEM/EDS analyses. This indicates good chemical compatibility under the selected joining conditions and suggests that the applied thermal profile does not trigger detrimental interfacial reactions. The small bright inclusions occasionally observed in Fig. 8a at the glass/AISI 441 interface are attributed to polishing artefacts caused by local dragging of metallic

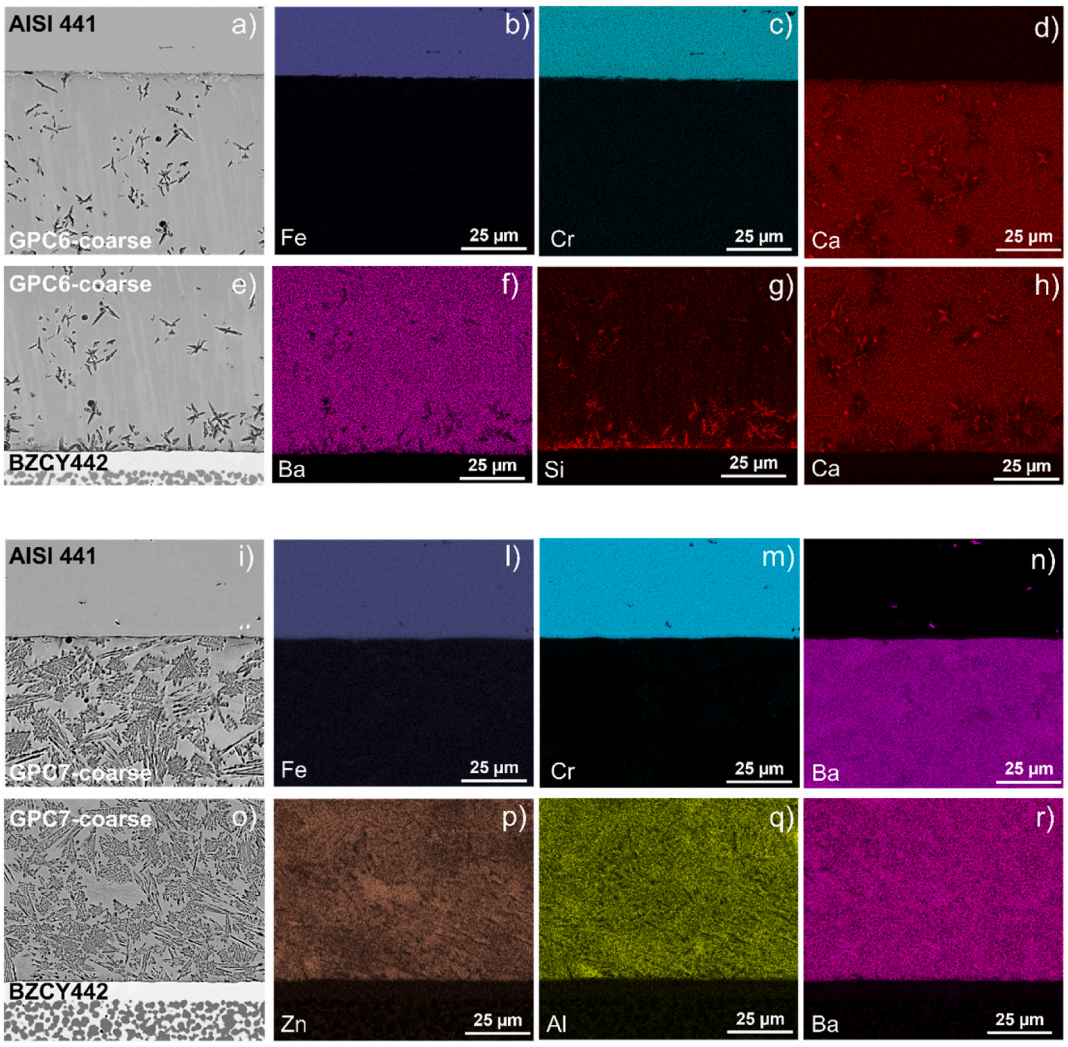


Fig. 8. Post-mortem SEM–EDS analysis of cross-sections of asymmetric ceramic/glass/metal joined samples fabricated under optimised joining conditions. Panels (a–h) refer to the sample joined with GPC6-coarse at 670 °C for 30 min under 0.005 MPa; panels (i–r) refer to the sample joined with GPC7-coarse at 690 °C for 30 min under 0.01 MPa. (a) SEM micrograph of the AISI 441/GPC6-coarse interface; (b–d) corresponding EDS maps of Fe, Cr, and Ca. (e) SEM micrograph of the GPC6-coarse/BZCY442 interface; (f–h) corresponding EDS maps of Ba, Si, and Ca. (i) SEM micrograph of the AISI 441/GPC7-coarse interface; (l–n) corresponding EDS maps of Fe, Cr, and Ba. (o) SEM micrograph of the GPC7-coarse/BZCY442 interface; (p–r) corresponding EDS maps of Zn, Al, and Ba.

fragments during sample preparation, with no evidence of associated interdiffusion or interfacial degradation.

Fig. 8i shows the AISI 441/GPC7-coarse interface, while Fig. 8o shows the GPC7-coarse/BZCY442 interface. Also in this case, the glass shows good adhesion and continuity at both interfaces. The sealant is dense and crack-free, with no relevant residual porosity observed, consistent with the corresponding symmetrically joined samples. Fig. 8l and m shows the EDS maps of Fe and Cr, respectively. Again, within the spatial resolution of EDS, no detectable Fe or Cr diffusion from AISI 441 into the glass is observed after joining. Although BCZY442 contains Ba, the electrolyte in Fig. 8r appears darker because the Ba signal is stronger in the glass, resulting in a lower relative contrast in the electrolyte.

Compared with GPC6-coarse, GPC7-coarse exhibits a higher degree of crystallisation, with a more homogeneous distribution of crystalline features within the glass matrix and no evident preferential formation at the interfaces. This is consistent with the identification of β–BaB_2O_4 by XRD. The EDS maps indicate that the crystalline phase is depleted in Zn (Fig. 8p) and Al (Fig. 8q), while no significant Ba depletion is observed between the glass matrix and the crystalline regions (Fig. 8n and r). Also, for GPC7-coarse, no microstructural evidence of interfacial instability or interdiffusion is observed at the glass/BZCY442 interface within the SEM/EDS resolution, confirming chemical compatibility under the selected joining conditions. Overall, both GPC6-coarse and GPC7-coarse retain a significant residual amorphous fraction after joining, which is higher for GPC6-coarse than for GPC7-coarse. The presence of a continuous glassy phase is relevant for sealant operation, as it can support self-healing under PCEC conditions. This aspect is particularly important in the presence of combined thermo-mechanical stresses from CTE mismatch and additional stresses associated with perovskite chemical expansion upon hydration.

4. Conclusions

Developing reliable sealing solutions for the integration of large-area proton conducting electrolysis cells (PCECs) remains a major technological challenge for scale-up. In this work, two innovative borate-rich glass sealants were developed and systematically investigated for the integration of NiO-SZCY/BZCY442 PCEC half-cells with AISI 441 metallic interconnects. The proposed formulations belong to the B_2O_3–BaO–Al_2O_3–CaO–SrO–SiO_2 system and to the B_2O_3–BaO–SiO_2–Al_2O_3–CaO–SrO–ZnO–ZrO_2 system. Both compositions were tailored to provide viscous compliance at PCEC operating temperatures (500–600 °C) while enabling joining below 700 °C to limit interfacial reactivity. A comprehensive thermal and kinetic analysis, performed on

both fine and coarse powder fractions, enabled a detailed evaluation of densification, viscous flow, and crystallisation behaviour. Both glasses exhibited high densification and sufficient viscous flow within the targeted joining window, ensuring effective wetting and consolidation of the sealing interfaces. Crystallisation was predominantly surface-controlled in both systems; however, the ZnO–ZrO_2-containing glass exhibited a lower crystallisation activation energy (201–259 kJ mol^{-1}) than the ZnO–ZrO_2-free formulation (279–308 kJ mol^{-1}), indicating a higher crystallisation tendency. Based on these results, the joining process was optimised by systematically tuning peak temperature and applied pressure. Symmetric metal/glass/metal joined samples (50 mm × 50 mm) fabricated under optimised conditions exhibited excellent control of sealant geometry together with outstanding gas-tightness, with measured He leakage rates $<1 \times 10^{-9}$ mbar·L·s^{-1}. The most reliable joining conditions were identified as 670 °C for 30 min under 0.005 MPa for the ZnO–ZrO_2-free glass and 690 °C for 30 min under 0.01 MPa for the ZnO–ZrO_2-containing formulation. The same joining protocols applied to ceramic/glass/metal assemblies with 30 mm-diameter half-cells yielded similarly promising results, with pressure drops below 2 mbar after 5 min and a final sealant thickness of approximately 200 μm. Post-mortem analyses confirmed dense, crack-free interfaces with strong adhesion and good chemical compatibility. Overall, these results demonstrate that properly designed borate-rich glass sealants enable rapid joining at relatively low temperatures, delivering excellent wetting and hermetic sealing, even in the presence of predominantly surface-driven crystallisation (more pronounced for the ZnO–ZrO_2-containing system). Although glass sealants for PCEC have been previously reported, sealants of this type and equally systematic joining optimisation supported by quantitative gas-tightness validation remain scarce, underscoring the relevance of this work for reliable intermediate-temperature PCEC sealing and future SRU-level integration. Long-term ageing and thermal-cycling tests under PCEC-relevant operating conditions will be performed in future work to assess the thermal stability, crystallisation evolution, and sealing durability of the developed glass systems.

Declaration of generative AI and AI-assisted technologies in the writing process

During the preparation of this work the author(s) used ChatGPT in order to smooth and grammatically correct the written text. After using this tool/service, the author(s) reviewed and edited the content as needed and take(s) full responsibility for the content of the publication.

Funding

- SNAM, Ordine di Lavoro Nr. 7800098086 del 21/12/2023, Contr. 5000005095 del 15.12.2022.
- PROGETTI DI RICERCA FONDAMENTALE PER L'IDROGENO NELL'AMBITO DEL PNRR – M2C2 LINEA DI INVESTIMENTO 3.5 Bando A, prot. n. 59540 identificativo RSH2A_000027 "Innovative Proton Conductive Electrolysis Cells (PCECs) for Hydrogen Production (INNOPHY)".

CRediT authorship contribution statement

Francesco Da Prato: Conceptualization, Data curation, Formal analysis, Investigation, Methodology, Validation, Visualization, Writing – original draft, Writing – review & editing. **Sonja-Michaela Groß-Barsnick:** Conceptualization, Data curation, Formal analysis, Investigation, Methodology, Supervision, Validation, Visualization, Writing – review & editing. **Simone Anelli:** Conceptualization, Data curation, Methodology, Supervision, Writing – review & editing. **Wendelin Deibert:** Conceptualization, Data curation, Methodology, Supervision, Validation, Visualization, Writing – review & editing. **Wilhelm Albert Meulenberg:** Funding acquisition, Project administration, Resources, Supervision, Validation, Writing – review & editing. **Sandrine Ricote:** Funding acquisition, Project administration, Resources, Supervision, Validation, Writing – review & editing. **Massimo Santarelli:** Funding acquisition, Project administration, Resources, Supervision, Validation, Writing – review & editing. **Federico Smeacetto:** Funding acquisition, Project administration, Resources, Supervision, Validation, Writing – review & editing.

Declaration of competing interest

The authors declare that they have no known competing financial interests or personal relationships that could have appeared to influence the work reported in this paper.

Acknowledgment

The authors acknowledge the collaborations between Forschungszentrum Jülich GmbH, IMD-2 and ITE; HyET NoCarbon and Politecnico di Torino.

Appendix A. Supplementary data

Supplementary data to this article can be found online at https://doi.org/10.1016/j.jpowsour.2026.240816.

Data availability

Data will be made available on request.

References

[1] R. Angelico, F. Giametta, B. Bianchi, P. Catalano, Green hydrogen for energy transition: a critical perspective, Energies 18 (2025), https://doi.org/10.3390/en18020404.
[2] C. Breyer, G. Lopez, D. Bogdanov, P. Laaksonen, The role of electricity-based hydrogen in the emerging power-to-X economy, Int. J. Hydrogen Energy 49 (2024) 351–359, https://doi.org/10.1016/j.ijhydene.2023.08.170.
[3] M. Genovese, A. Schlüter, E. Scionti, F. Piraino, O. Corigliano, P. Fragiacomo, Power-to-hydrogen and hydrogen-to-X energy systems for the industry of the future in Europe, Int. J. Hydrogen Energy 48 (2023) 16545–16568, https://doi.org/10.1016/j.ijhydene.2023.01.194.
[4] M. Fallah Vostakola, H. Ozcan, R.S. El-Emam, B. Amini Horri, Recent advances in high-temperature steam electrolysis with solid oxide electrolysers for green hydrogen production, Energies 16 (2023) 3327, https://doi.org/10.3390/en16083327.
[5] S. Shiva Kumar, H. Lim, An overview of water electrolysis technologies for green hydrogen production, Energy Rep. 8 (2022) 13793–13813, https://doi.org/10.1016/j.egyr.2022.10.127.
[6] D. Ferrero, A. Lanzini, M. Santarelli, P. Leone, A comparative assessment on hydrogen production from low- and high-temperature electrolysis, Int. J. Hydrogen Energy 38 (2013) 3523–3536, https://doi.org/10.1016/j.ijhydene.2013.01.065.
[7] I. Sreedhar, B. Agarwal, P. Goyal, S.A. Singh, Recent advances in material and performance aspects of solid oxide fuel cells, J. Electroanal. Chem. 848 (2019) 113315, https://doi.org/10.1016/j.jelechem.2019.113315.
[8] S.E. Wolf, F.E. Winterhalder, V. Vibhu, L.G.J. de Haart, O. Guillon, R.A. Eichel, N. H. Menzler, Solid oxide electrolysis cells - current material development and industrial application, J. Mater. Chem. A 11 (2023) 17977–18028, https://doi.org/10.1039/d3ta02161k.
[9] G. Min, S. Choi, J. Hong, A review of solid oxide steam-electrolysis cell systems: thermodynamics and thermal integration, Appl. Energy 328 (2022) 120145, https://doi.org/10.1016/j.apenergy.2022.120145.
[10] M. Riegraf, M. Riedel, S.H. Jensen, S. Santhanam, S.A. Ansar, M. Heddrich, Solid oxide electrolysis cells: bridging materials development and process system engineering for gigawatt-scale applications. https://doi.org/10.48550/arXiv.2512.16488, 2025.
[11] E.N. Aminaho, N.S. Aminaho, F. Aminaho, Techno-economic assessments of electrolyzers for hydrogen production, Appl. Energy 399 (2025) 126515, https://doi.org/10.1016/j.apenergy.2025.126515.
[12] L.A. Jolaoso, I.T. Bello, O.A. Ojelade, A. Yousuf, C. Duan, P. Kazempoor, Operational and scaling-up barriers of SOEC and mitigation strategies to boost H2 production- a comprehensive review, Int. J. Hydrogen Energy 48 (2023) 33017–33041, https://doi.org/10.1016/j.ijhydene.2023.05.077.
[13] F. Ferrete, A. Molina, G.M. Cabello González, Á. Moreno-Racero, H. Olmedo, A. Iranzo, Solid oxide electrolyzers process integration: a comprehensive review, Processes 13 (2025) 2656, https://doi.org/10.3390/pr13082656.
[14] K.J. Yoon, S. Lee, S.-Y. Park, N.Q. Minh, Advances in high-temperature solid oxide electrolysis technology for clean hydrogen and chemical production: materials,

cells, stacks, systems and economics, Prog. Mater. Sci. 154 (2025) 101520, https://doi.org/10.1016/j.pmatsci.2025.101520.
[15] C. Duan, J. Huang, N. Sullivan, R. O'Hayre, Proton-conducting oxides for energy conversion and storage, Appl. Phys. Rev. 7 (2020) 011314, https://doi.org/10.1063/1.5135319.
[16] H.I. Ji, J.H. Lee, J.W. Son, K.J. Yoon, S. Yang, B.K. Kim, Protonic ceramic electrolysis cells for fuel production: a brief review, J. Korean Ceram. Soc. 57 (2020) 480–494, https://doi.org/10.1007/s43207-020-00059-4.
[17] L.Q. Le, C. Meisel, C.H. Hernandez, J. Huang, Y. Kim, R. O'Hayre, N.P. Sullivan, Performance degradation in proton-conducting ceramic fuel cell and electrolyzer stacks, J. Power Sources 537 (2022) 231356, https://doi.org/10.1016/j.jpowsour.2022.231356.
[18] B. Seong, J. Yun, S. Choi, High-performance and excellent thermal cycling stability of reversible protonic ceramic cells enabled by a promising Sr/Co-free $PrNi_{0.5}Fe_{0.5}O_{3-\delta}$ air electrode, J. Mater. Chem. A 12 (2024) 32084–32094, https://doi.org/10.1039/D4TA05359A.
[19] L. Kwati, K. Miyazaki, C. Dellen, M.E. Ivanova, W. Deibert, J. Wolter, W. A. Meulenberg, O. Guillon, V. Vediyappan, T. Ishihara, H. Matsumoto, Toward highly efficient protonic electrolysis cells for large-scale hydrogen production at moderate temperatures, Mater. Adv. 6 (2025) 3253–3263, https://doi.org/10.1039/D5MA00028A.
[20] A. Moranti, F. Riva, T.M. Bachmann, J. Dailly, Environmental performance of a metal-supported protonic ceramic cell and an electrolyte-supported solid oxide cell for steam electrolysis, Int. J. Hydrogen Energy 92 (2024) 1284–1297, https://doi.org/10.1016/j.ijhydene.2024.10.221.
[21] F.J.A. Loureiro, N. Nasani, G.S. Reddy, N.R. Munirathnam, D.P. Fagg, A review on sintering technology of proton conducting BaCeO3-BaZrO3 perovskite oxide materials for protonic ceramic fuel cells, J. Power Sources 438 (2019) 226991, https://doi.org/10.1016/j.jpowsour.2019.226991.
[22] Y. Wang, Y. Ling, B. Wang, G. Zhai, G. Yang, Z. Shao, R. Xiao, T. Li, A review of progress in proton ceramic electrochemical cells: material and structural design, coupled with value-added chemical production, Energy Environ. Sci. 16 (2023) 5721–5770, https://doi.org/10.1039/D3EE03121G.
[23] X. Yang, Z. Wang, G. Li, Y. Zhou, C. Sun, L. Bi, Sc-doped Ba0.5Sr0.5Co0.8Fe0.2O3-δ cathodes for protonic ceramic fuel cells, Ceram. Int. 50 (2024) 40375–40383, https://doi.org/10.1016/j.ceramint.2024.03.085.
[24] L. Wu, J. Sun, H. Qi, B. Tu, C. Xiong, F. Chen, P. Qiu, Boosting steam tolerance and electrochemical performance of an $La_{0.6}Sr_{0.4}Co_{0.2}Fe_{0.8}O_{3-\delta}$ -based air electrode for protonic ceramic electrochemical cells, J. Mater. Chem. A 12 (2024) 25979–25987, https://doi.org/10.1039/D4TA03706E.
[25] L.Q. Le, C.H. Hernandez, M.H. Rodriguez, L. Zhu, C. Duan, H. Ding, R.P. O'Hayre, N.P. Sullivan, Proton-conducting ceramic fuel cells: scale up and stack integration, J. Power Sources 482 (2021) 228868, https://doi.org/10.1016/j.jpowsour.2020.228868.
[26] Z. Zakaria, Z. Awang Mat, S.H. Abu Hassan, Y. Boon Kar, A review of solid oxide fuel cell component fabrication methods toward lowering temperature, Int. J. Energy Res. 44 (2020) 594–611, https://doi.org/10.1002/er.4907.
[27] R. Wang, Z. Sun, J.P. Choi, S.N. Basu, J.W. Stevenson, M.C. Tucker, Ferritic stainless steel interconnects for protonic ceramic electrochemical cell stacks: oxidation behavior and protective coatings, Int. J. Hydrogen Energy 44 (2019) 25297–25309, https://doi.org/10.1016/j.ijhydene.2019.08.041.
[28] J. Gao, X. Si, B. Yang, H. Yuan, M. Zheng, C. Li, J. Qi, J. Cao, TiO2 containing glass sealant for protonic ceramic fuel cell applications: microstructure, strength and stability studied in sealing of BaZr0.1Ce0.7Y0.1Yb0.1O3-δ electrolyte to crofer 22H interconnect, Ceram. Int. (2024), https://doi.org/10.1016/j.ceramint.2024.10.035.
[29] VDM Metals, VDM Crofer 22 APU Data Sheet, https://www.vdmmetals.com/fileadmin/user_upload/Downloads/Data_Sheets/Data_Sheet_VDM_Crofer_22_APU.pdf, (accessed 22 April 2026)..
[30] ATI, ATI 441 HP™ Ferritic Stainless Steel. https://www.atimaterials.com/Products/Pages/ati-441-hp.aspx, (accessed 22 April 2026)..
[31] A. Løken, S. Ricote, S. Wachowski, Thermal and chemical expansion in proton ceramic electrolytes and compatible electrodes, Crystals 8 (2018), https://doi.org/10.3390/cryst8090365.
[32] K.L. Ley, M. Krumpelt, R. Kumar, J.H. Meiser, I. Bloom, Glass-ceramic sealants for solid oxide fuel cells: part I. Physical properties, J. Mater. Res. 11 (1996) 1489–1493, https://doi.org/10.1557/JMR.1996.0185.
[33] J.W. Fergus, Sealants for solid oxide fuel cells, J. Power Sources 147 (2005) 46–57, https://doi.org/10.1016/j.jpowsour.2005.05.002.
[34] F. Smeacetto, A. Chrysanthou, A.G. Sabato, H. Javed, S.D. la Pierre, M. Salvo, M. Ferraris, Glass-to-metal seals for solid oxide cells at the Politecnico di Torino, an overview, Int. J. Appl. Ceram. Technol. 19 (2022) 1017–1028, https://doi.org/10.1111/ijac.13949.
[35] K. Singh, T. Walia, Review on silicate and borosilicate-based glass sealants and their interaction with components of solid oxide fuel cell, Int. J. Energy Res. 45 (2021) 20559–20582, https://doi.org/10.1002/er.7161.
[36] M.K. Mahapatra, K. Lu, Glass-based seals for solid oxide fuel and electrolyzer cells - a review, materials science and engineering R, Report 67 (2010) 65–85, https://doi.org/10.1016/j.mser.2009.12.002.
[37] S. Rodríguez-López, J. Malzbender, V.M. Justo, F.C. Serbena, S.M. Groß-Barsnick, M.J. Pascual, Thermo-mechanical stability and gas-tightness of glass-ceramics joints for SOFC in the system MgO-BaO/SrO-B2O3-SiO2, Front. Mater. 7 (2020) 19, https://doi.org/10.3389/fmats.2020.00019.
[38] S. Rodríguez-López, M. Pascual, Sintering/crystallization and viscosity of sealing glass-ceramics, Crystals 11 (2021) 737, https://doi.org/10.3390/cryst11070737.
[39] R. Voivenel, L. Montagne, F.O. Méar, Alkali-free glass seals compositions for electrochemical devices, Open Ceram. 26 (2026) 100965, https://doi.org/10.1016/j.oceram.2026.100965.
[40] I. Ritucci, K. Agersted, P. Zielke, A.C. Wulff, P. Khajavi, F. Smeacetto, A.G. Sabato, R. Kiebach, A Ba-free sealing glass with a high coefficient of thermal expansion and excellent interface stability optimized for SOFC/SOEC stack applications, Int. J. Appl. Ceram. Technol. 15 (2018) 1011–1022, https://doi.org/10.1111/ijac.12853.
[41] J. Schilm, A. Rost, H. Javed, M. Poetschke, Stability of glass ceramic sealants in atmospheres with increased water contents, ECS Trans. 111 (2023) 2341–2350, https://doi.org/10.1149/11106.2341ecst.
[42] S. Rodríguez-López, V.A.C. Haanappel, A. Durán, F. Muñoz, G.C. Mather, M. J. Pascual, S.M. Gross-Barsnick, Glass–ceramic seals in the system MgO BaO B 2 O 3 SiO 2 operating under simulated SOFC conditions, Int. J. Hydrogen Energy 41 (2016) 15335–15345, https://doi.org/10.1016/j.ijhydene.2016.07.051.
[43] H. Javed, A.G. Sabato, M. Mansourkiaei, D. Ferrero, M. Santarelli, K. Herbrig, C. Walter, F. Smeacetto, Glass-ceramic sealants for SOEC: thermal characterization and electrical resistivity in dual atmosphere, Energies 13 (2020) 3682, https://doi.org/10.3390/en13143682.
[44] A. Baggio, D. Dalmazzo, F. D'Isanto, E. Santagata, D. Basso, D. Gaia, M. Salvo, F. Smeacetto, Optimizing rheological behavior of glass-based sealant inks for robocasting deposition: a design of experiment approach, Mater. Des. 251 (2025) 113678, https://doi.org/10.1016/j.matdes.2025.113678.
[45] W. Zhang, X. Wang, Y. Dong, J. Yang, J. Pu, B. Chi, L. Jian, Development of flexible ceramic-glass seals for intermediate temperature planar solid oxide fuel cell, Int. J. Hydrogen Energy 41 (2016) 6036–6044, https://doi.org/10.1016/j.ijhydene.2016.02.120.
[46] A. De Pablos-Martín, S. Rodríguez-López, M.J. Pascual, Processing technologies for sealing glasses and glass-ceramics, Int. J. Appl. Glass Sci. 11 (2020) 552–568, https://doi.org/10.1111/ijag.15107.
[47] F. Da Prato, S. Anelli, A. Moranti, D. Ferrero, M. Santarelli, F. Smeacetto, Progress in the study of glass-based systems as sealants for proton ceramic electrolysis cell assembly, Int. J. Hydrogen Energy 140 (2025) 119–130, https://doi.org/10.1016/J.IJHYDENE.2025.05.286.
[48] S. Anelli, A. Baggio, D. Ferrero, D. Schmider, J. Dailly, M. Santarelli, F. Smeacetto, Characterization and testing of glass-ceramic sealants for protonic ceramic electrolysis cells applications, Ceram. Int. 50 (2024) 17520–17531, https://doi.org/10.1016/j.ceramint.2024.02.240.
[49] G. Hudish, A. Manerbino, W.G. Coors, S. Ricote, Chemical expansion in BaZr0.9−xCexY0.1O3−δ (X = 0 and 0.2) upon hydration determined by high-temperature X-ray diffraction, J. Am. Ceram. Soc. 101 (2018) 1298–1309, https://doi.org/10.1111/JACE.15275.
[50] J. Gao, X. Si, M. Li, W. Zhao, C. Li, J. Qi, J. Cao, A novel non-crystallizing Na2O-K2O-TiO2 silicate glass sealant for protonic ceramic fuel cell applications, Ceram. Int. 50 (2024) 49972–49978, https://doi.org/10.1016/j.ceramint.2024.09.342.
[51] J. Gao, X. Si, B. Yang, M. Li, C. Li, J. Qi, J. Cao, Improving the stability of BaZr0.1Ce0.7Y0.1Yb0.1O3-δ/Crofer 22 H glass-sealed joints in humid oxidizing environments with a Mn-Co spinel coating, Ceram. Int. (2024), https://doi.org/10.1016/j.ceramint.2024.10.342.
[52] J. Gao, X. Si, H. Jiang, H. Yang, W. Zhang, C. Li, J. Qi, J. Cao, Effect of TiO2 on crystallization and sealing behavior of Na2O-K2O-TiO2-SiO2-Al2O3-ZnO glass sealant for PCFCs, Ceram. Int. (2025) 1–10, https://doi.org/10.1016/j.ceramint.2025.01.423.
[53] K. Leonard, W. Deibert, M.E. Ivanova, W.A. Meulenberg, T. Ishihara, H. Matsumoto, Processing ceramic proton conductor membranes for use in steam electrolysis, Membranes 10 (2020) 339, https://doi.org/10.3390/membranes10110339.
[54] H. Wang, X. Xu, D. Mo, H. Zhang, T. Zheng, Y. Guo, J. Lv, Effect of ZnO on the microstructure and mechanical properties of lithium disilicate glass ceramics, Ceram. Int. (2026) S027288422600180X, https://doi.org/10.1016/j.ceramint.2026.01.173.
[55] A. Zawada, M. Lubas, A. Nowak, Experimental vs. theoretical viscosity determination of aluminosilicate glasses, Materials 16 (2023), https://doi.org/10.3390/ma16175789.
[56] K. Matusita, S. Sakka, Kinetic study of crystallization of glass by differential thermal analysis—criterion on application of kissinger plot, J. Non-Cryst. Solids 38–39 (1980) 741–746, https://doi.org/10.1016/0022-3093(80)90525-6.
[57] T. Ozawa, Kinetics of non-isothermal crystallization, Polymer 12 (1971) 150–158, https://doi.org/10.1016/0032-3861(71)90041-3.
[58] H.E. Kissinger, Variation of peak temperature with heating rate in differential thermal analysis, J. Res. Natl. Bur. Stan. 57 (1956) 217, https://doi.org/10.6028/jres.057.026.
[59] A.A. Francis, R.D. Rawlings, R. Sweeney, A.R. Boccaccini, Crystallization kinetic of glass particles prepared from a mixture of coal ash and soda-lime cullet glass, J. Non-Cryst. Solids 333 (2004) 187–193, https://doi.org/10.1016/j.jnoncrysol.2003.09.048.
[60] A. Karamanov, I. Avramov, L. Arrizza, R. Pascova, I. Gutzow, Variation of avrami parameter during non-isothermal surface crystallization of glass powders with different sizes, J. Non-Cryst. Solids 358 (2012) 1486–1490, https://doi.org/10.1016/j.jnoncrysol.2012.04.003.
[61] E. Ercenk, The crystallization kinetics of the CaO-SiO2-P2O5-MgO-Al2O3 base glass system, J. Non-Cryst. Solids 387 (2014) 101–106, https://doi.org/10.1016/j.jnoncrysol.2014.01.017.
[62] D. Federmann, S.M. Groß-Barsnick, H.R. Zerfass, "Forschungszentrum Jülich GmbH. Method for producing a solder glass green seal." METHOD FOR PRODUCING A SOLDER GLASS GREEN SEAL, EUEP 2 991 942 B1 (2014) 991942B1.

[63] M. Hilger, T. Krogsgaard, S.-M. Groß-Barsnick, D. Sebold, S. Shrikanth, J. Froitzheim, C. Lenser, N.H. Menzler, Electrophoretic deposition of protective spinel coatings for solid oxide cell interconnects – towards stack integration, J. Electrochem. Soc. 173 (2026) 034509, https://doi.org/10.1149/1945-7111/ae3ebb.
[64] O.L.G. Alderman, N.S. Tagiara, I. Slagle, R.M. Gabrielsson, P. Boggs, M. Wagner, A. Rossini, S. John, L. Rocha, R.M. Wilson, H. Hawbaker, S.W. Martin, A. C. Hannon, E.I. Kamitsos, S.A. Feller, A review of the fraction of four-coordinated boron in binary borate glasses and melts, Rep. Prog. Phys. 88 (2025), https://doi.org/10.1088/1361-6633/adc69c.
[65] E.D. Zanotto, D.R. Cassar, The microscopic origin of the extreme glass-forming ability of albite and B2O3, Sci. Rep. 7 (2017), https://doi.org/10.1038/srep43022.
[66] N.J. Clayden, S. Esposito, A. Aronne, P. Pernice, Solid state 11B NMR study of glasses near the barium metaborate stoichiometry, J. Non-Cryst. Solids 249 (1999) 99–105, https://doi.org/10.1016/S0022-3093(99)00335-X.
[67] C.S. Pavan Kumar, S. Pratap, C.S. Sumuka, N. Sivasankara Reddy, Review on the structure of borate glasses by raman spectroscopic technique, Ceram. Int. 52 (2026) 1359–1382, https://doi.org/10.1016/j.ceramint.2025.12.004.
[68] J. Jiusti, E.D. Zanotto, S.A. Feller, H.J. Austin, H.M. Detar, I. Bishop, D. Manzani, Y. Nakatsuka, Y. Watanabe, H. Inoue, Effect of network formers and modifiers on the crystallization resistance of oxide glasses, J. Non-Cryst. Solids 550 (2020), https://doi.org/10.1016/j.jnoncrysol.2020.120359.
[69] M.J. Snyder, M.G. Mesko, J.E. Shelby, Volatilization of boron from E-glass melts, J. Non-Cryst. Solids 352 (2006) 669–673, https://doi.org/10.1016/j.jnoncrysol.2005.11.068.
[70] I.Yu Archakov, V.L. Stolyarova, M.M. Shultz, Relative volatility of borosilicate glasses: a mass spectrometric study, Rapid Commun. Mass Spectrom. 12 (1998) 1330–1334, https://doi.org/10.1002/(SICI)1097-0231(19981015)12:19%3C1330::AID-RCM294%3E3.0.CO;2-Z.
[71] J.P. Singh, N.P. Bansal, T. Goto, J. Lamon, S.R. Choi, M.M. Mahmoud, G. Link (Eds.), Processing and Properties of Advanced Ceramics and Composites IV, first ed., Wiley, 2012 https://doi.org/10.1002/9781118491867.
[72] M.J. Pascual, A. Durán, M.O. Prado, A new method for determining fixed viscosity points of glasses, Phys. Chem. Glasses 46 (2005) 512–520.
[73] B. Agea-Blanco, S. Reinsch, R. Müller, Sintering and foaming of barium silicate glass powder compacts, Front. Mater. 3 (2016), https://doi.org/10.3389/fmats.2016.00045.
[74] F. D'Isanto, A. Baggio, M. Salvo, D. Basso, D. Gaia, F. Smeacetto, Glass-based sealants for joining α to β''-Al2O3 in Na–Zn batteries, Ceram. Int. 50 (2024) 14542–14549, https://doi.org/10.1016/j.ceramint.2024.01.367.
[75] K.S. Weil, The state-of-the-art in sealing technology for solid oxide fuel cells, JOM 58 (2006) 37–44, https://doi.org/10.1007/s11837-006-0052-6.
[76] M. Erol, S. Küçükbayrak, A. Ersoy-Meriçboyu, The application of differential thermal analysis to the study of isothermal and non-isothermal crystallization kinetics of coal fly ash based glasses, J. Non-Cryst. Solids 355 (2009) 569–576, https://doi.org/10.1016/j.jnoncrysol.2009.01.023.
[77] L. Deng, W. Lu, Z. Zhang, Z. Fu, H. Li, H. Chen, Y. Du, Y. Ma, W. Wang, Crystallization behavior and structure of CaO–MgO–Al2O3–SiO2 glass ceramics prepared from Cr-bearing slag, Mater. Chem. Phys. 261 (2021), https://doi.org/10.1016/j.matchemphys.2021.124249.
[78] M. Tao, J. Feng, R. Li, C. Guan, J. Pu, B. Chi, Effect of particle size distribution on crystallization behavior of glass-based seals in reversible solid oxide cells, J. Am. Ceram. Soc. 105 (2022) 6593–6603, https://doi.org/10.1111/jace.18608.
[79] A.G. Sabato, M. Salvo, A. De Miranda, F. Smeacetto, Crystallization behaviour of glass-ceramic sealant for solid oxide fuel cells, Mater. Lett. 141 (2015) 284–287, https://doi.org/10.1016/j.matlet.2014.11.128.
[80] A.A.S. Lopes, R.S. Soares, M.M.A. Lima, R.C.C. Monteiro, Glass transition and crystallization kinetics of a barium borosilicate glass by a non-isothermal method, J. Appl. Phys. 115 (2014) 043516, https://doi.org/10.1063/1.4863334.
[81] YuG. Lyagaeva, D.A. Medvedev, A.K. Demin, P. Tsiakaras, O.G. Reznitskikh, Thermal expansion of materials in the barium cerate-zirconate system, Phys. Solid State 57 (2015) 285–289, https://doi.org/10.1134/S1063783415020250.
[82] S.K. Filatov, N.V. Nikolaeva, R.S. Bubnova, I.G. Polyakova, Thermal expansion of β-BaB2O4 and BaB 4O7 borates, Glass Phys. Chem. 32 (2006) 471–478, https://doi.org/10.1134/S1087659606040110.
[83] C. Malinverni, M. Salvo, A. De Zanet, F. D'Isanto, F. Smeacetto, P. Bertrand, G. Puchas, S. Schafföner, V. Casalegno, Glass-ceramics for joining oxide-based ceramic matrix composites (Al2O3f/Al2O3-ZrO2) operating under direct flame exposure, J. Eur. Ceram. Soc. 43 (2023) 3621–3629, https://doi.org/10.1016/j.jeurceramsoc.2023.02.019.
[84] F. D'Isanto, F. Smeacetto, H.P. Martin, R. Sedlák, M. Lisnichuk, A. Chrysanthou, M. Salvo, Development and characterisation of a Y2Ti2O7-based glass-ceramic as a potential oxidation protective coating for titanium suboxide (TiOx), Ceram. Int. 47 (2021) 19774–19783, https://doi.org/10.1016/j.ceramint.2021.03.316.
[85] L. Fang, H. Liu, D. Zhao, H. Yang, D. Tang, T. Zhang, Reducing the reaction between boron-containing sealing glass-ceramics and lanthanum-containing cathode: effect of Bi2O3, J. Eur. Ceram. Soc. 34 (2014) 4463–4468, https://doi.org/10.1016/j.jeurceramsoc.2014.07.006.
[86] K. Eichler, G. Solow, P. Otschik, W. Schaffrath, BAS (BaO·Al2O3·SiO2)-glasses for high temperature applications, J. Eur. Ceram. Soc. 19 (1999) 1101–1104, https://doi.org/10.1016/S0955-2219(98)00382-3.
[87] X. Li, E. Yazhenskikh, S.M. Groß-Barsnick, S. Baumann, P. Behr, W. Deibert, T. Koppitz, M. Müller, W.A. Meulenberg, G. Natour, Crystallization behavior of BaO–CaO–SiO2–B2O3 glass sealant and adjusting its thermal properties for oxygen transport membrane joining application, J. Eur. Ceram. Soc. 43 (2023) 2541–2552, https://doi.org/10.1016/j.jeurceramsoc.2022.12.063.
[88] A. Ali, Y.W. Chiang, R.M. Santos, X-ray diffraction techniques for mineral characterization: a review for engineers of the fundamentals, applications, and research directions, Minerals 12 (2022) 205, https://doi.org/10.3390/min12020205.